LITHOS 440-441 (2023) 107023

Contents lists available at ScienceDirect

LITHOS

journal homepage: www.elsevier.com/locate/lithos

The Sanandaj-Sirjan Zone (W. Iran) was a Jurassic passive continental margin: Evidence from igneous rocks of the Songhor area

Fatemeh Nouri [a,*], Hossein Azizi [a], Robert J. Stern [b], Yoshihiro Asahara [c]

[a] Department of Mining Engineering, Faculty of Engineering, University of Kurdistan, Sanandaj, Iran
[b] Geosciences Department, University of Texas at Dallas, Richardson, TX 75083-0688, USA
[c] Department of Earth and Environmental Sciences, Graduate School of Environmental Studies, Nagoya University, Nagoya, Japan

ARTICLE INFO

Keywords:
Jurassic magmatism
Passive margin
Rifted margin
Sanandaj Sirjan Zone
Transitional crust

ABSTRACT

It is important to understand the Jurassic tectonic setting of SW Eurasia, and the igneous rocks of the Sanandaj-Sirjan zone in SW Iran provide critical evidence. Bimodal volcanic and hypabyssal rocks exposed around Songhor in the central part of the Sanandaj-Sirjan zone have zircon U-Pb crystallization ages of 156 Ma for felsic and 153 to 146 Ma for mafic rocks. Felsic volcanic and subvolcanic rocks with affinity to A-type granite have high SiO_2 (62.6 to 73.9 wt%) and total alkalis ($K_2O + Na_2O$ = 5.1–9.8 wt%), low MgO (0.1–3.1 wt%) and slightly positive εNd(t) (+0.6 to +3.8) and moderate $^{87}Sr/^{86}Sr$(i) ratios (0.7041 to 0.7061). The mafic rocks (basalt and micro gabbro/dolerite) with lower contents of SiO_2 (47.0 to 54.6 wt%), high MgO (4.1 to 10.7 wt%) with variable Na_2O (2.0–5.9 wt%) and K_2O (0.1–2.6 wt%) can be divided into two groups based on TiO_2 contents: 1) low-Ti and 2) high-Ti. The low-Ti group has 0.14 to 0.62 wt% TiO_2 with εNd(t) = +3.2 to +5.8 and $^{87}Sr/^{86}Sr$(i) = 0.7032–0.7059. The high-Ti basalts have 1.4–1.6 wt% TiO_2 with εNd(t) = +1.2 to +4.2 and $^{87}Sr/^{86}Sr$(i) =0.7039 to 0.7057. The low-Ti suite is less fractionated, with Mg# between 55 and 74 compared to 43 to 63 for the high-Ti suite. Felsic rocks may have formed by remelting of underplated mafic rocks which were derived from sub-continental lithospheric mantle along with minor assimilation of continental crust in the early stage of extension. Thinning of continental lithosphere continued with increasing partial melting to produce high-Ti mafic melts early and low-Ti mafic melts in the late stage. Similar Sr-Nd isotope ratios for the mafic and felsic rocks with an 8–10 Ma interval between these two groups hint at gradual thinning of the continental lithosphere. This is consistent with formation of transitional crust of a passive continental margin between Neo-Tethys and Iran continental crust in Jurassic time.

1. Introduction

Bimodal magmatic suites can provide important information on crust-mantle interaction in different tectonic settings (Lyu et al., 2017). Bimodal magmatism is more frequent in intraplate extensional settings, such as oceanic and continental hot spots and continental rifts, whereas it is less common in mature arcs (Ayalew and Gibson, 2009). Understanding the petrogenesis of the mafic end-member of bimodal volcanic rocks is significant for unraveling the thermal state and composition of the mantle source, whereas the felsic end-member can provide evidence of crustal reworking (Ayalew and Gibson, 2009). A wide range of geological and geophysical data confirm that extensional thinning of the lithosphere related to bimodal magmatic activity and asthenospheric mantle upwelling are typical features of a continental rift. Thus, identifying and understanding bimodal magmatic rocks are important for recognizing continental rifts.

The Sanandaj-Sirjan Zone (SaSZ) of Iran is an important tectono-magmatic province, encompassing a SE-NW trending zone that is 50–100 km wide and 1200 km long (Stocklin and Nabavi, 1973). The SaSZ is bordered by the Zagros outer ophiolite belt to the SW and by the inner ophiolite belt in the NE (Stern et al., 2021). The SaSZ today is a key part of the Iran convergent margin but its origin and significance are controversial. SaSZ magmatic activity occurred in Middle Jurassic to Early Cretaceous (177–144 Ma) time and is considered by many to be a consequence of Neo-Tethys convergence and subduction (e.g., Azizi et al., 2011, 2015a, 2015b; Azizi and Asahara, 2013; Davoudian et al., 2008; Mahmoudi et al., 2011; Stocklin and Nabavi, 1973). However, the identification of slightly younger extensional basins (Stefano et al.,

* Corresponding author.
E-mail address: f.nourisandiani@gmail.com (F. Nouri).

https://doi.org/10.1016/j.lithos.2023.107023
Received 10 February 2022; Received in revised form 30 December 2022; Accepted 8 January 2023
Available online 13 January 2023

2018) supports an interpretation of Jurassic rifting. Furthermore, Hunziker et al. (2015) showed that SaSZ granites were generated in a Jurassic continental rift. Azizi et al. (2020a) considered 145 to 144 Ma OIB-like melts as the source of Jurassic basalts in the Ghorveh area. Zarasvandi et al. (2021) compared the lack of Cu mineralization of SaSZ Jurassic granites with significant mineralization of the younger Urumieh Dohktar magmatic arc (UDMA), concluding that SaSZ magmatic rocks do not show arc-type mineralization. As a result of these several lines of evidence, a propagating rift model (from SE to NW) was recently proposed for volcanic and intrusive rocks of the central SaSZ (Azizi and Stern, 2019).

This research presents new petrographic, whole rock chemistry, zircon U-Pb ages and Sr-Nd isotope ratios from poorly studied volcanic and hypabyssal rocks cropping out in the Songhor area of the central SaSZ (Figs. 1, 2). This research aims to (1) investigate their origin and magmatic processes, and (2) constrain the associated geodynamic processes and evolution of the region. These data in combination with pertinent available geological data are discussed in terms of petrogenesis and tectonic setting, which are crucial for understanding formation of Songhor volcanic and subvolcanic rocks, in particular, and the geological history of the SaSZ. Based on our findings we argue that these melts formed in the Jurassic at a volcanic rifted margin on the SW margin of Iran.

2. Geological setting and field observations

The SaSZ is one of the main magmato-tectonic zones in Iran. The SaSZ consists of metamorphosed and deformed supracrustal sequences associated with voluminous Jurassic intrusions and volcanic rocks.

The SaSZ is divided into northern, central, and southern parts (Fig. 1) (Azizi and Stern, 2019). The northern SaSZ (N-SaSZ) includes 600–500 Ma calc-alkaline granites, gneisses, and related rocks known as Cadomian basements, demonstrating that the N-SaSZ formed on Iran continental crust. Paleozoic granitoid magma injections at 350–330 Ma show affinity to A-type granite. The SaSZ and pre-Mesozoic basement was cut by Late Cretaceous granites and Paleogene granites and volcanics (Azizi et al., 2020a, 2020b; Gholipour et al., 2021). Late Cretaceous and younger igneous rocks formed at a convergent margin, following subduction initiation at ~95–100 Ma (Stern et al., 2021).

Central SaSZ (C-SaSZ) basement consists of deformed amphibolite and meta-granites and Early to Mid-Jurassic metamorphic and magmatic rocks, with protoliths thought to be submarine MORB and OIB-like volcanics (Azizi et al., 2018, 2020a; Tavakoli et al., 2021). C-SaSZ Early to Mid-Jurassic sequences include lavas (basalt, basaltic-andesite and andesite), subvolcanic bodies (micro-gabbro/dolerite to micro-diorite) and volcaniclastics (tuff, agglomerate and breccia) interbedded with marble, shale, slate and sandstone. These rocks suggest a magmatic continental rift that evolved into a marine basin (Azizi et al., 2018, 2020a; Tavakoli et al., 2021). C-SaSZ Jurassic and older rocks are unconformably covered by Early Cretaceous carbonates. Basement of

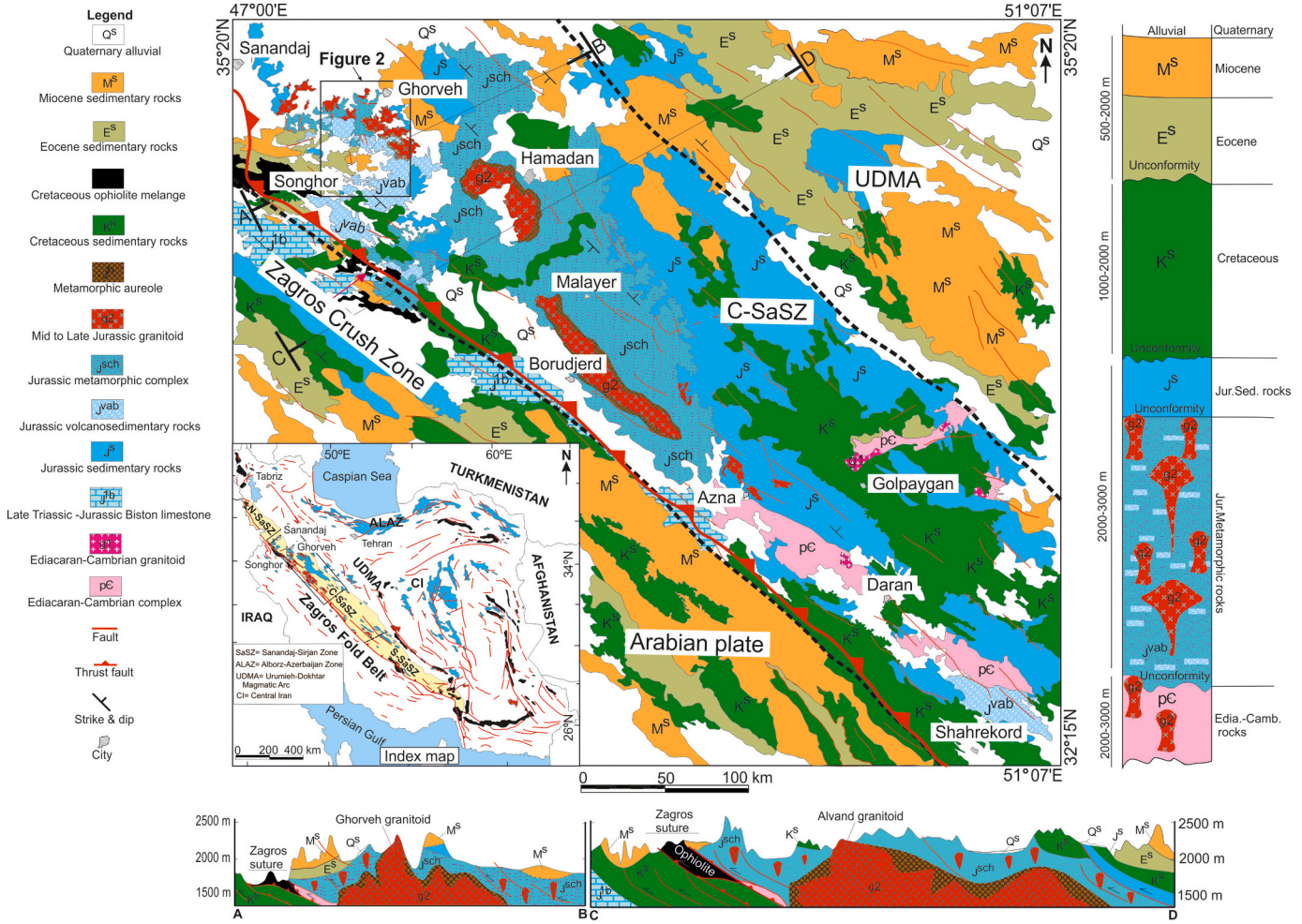

Fig. 1. Simplified geological map of western Iran, showing that the C-SaSZ, Zagros Fold Belt, and UDMA extend parallel to the Zagros Crush Zone (Stocklin and Nabavi, 1973). Inset is a simplified geological structural map of Iran (Stocklin and Nabavi, 1973).

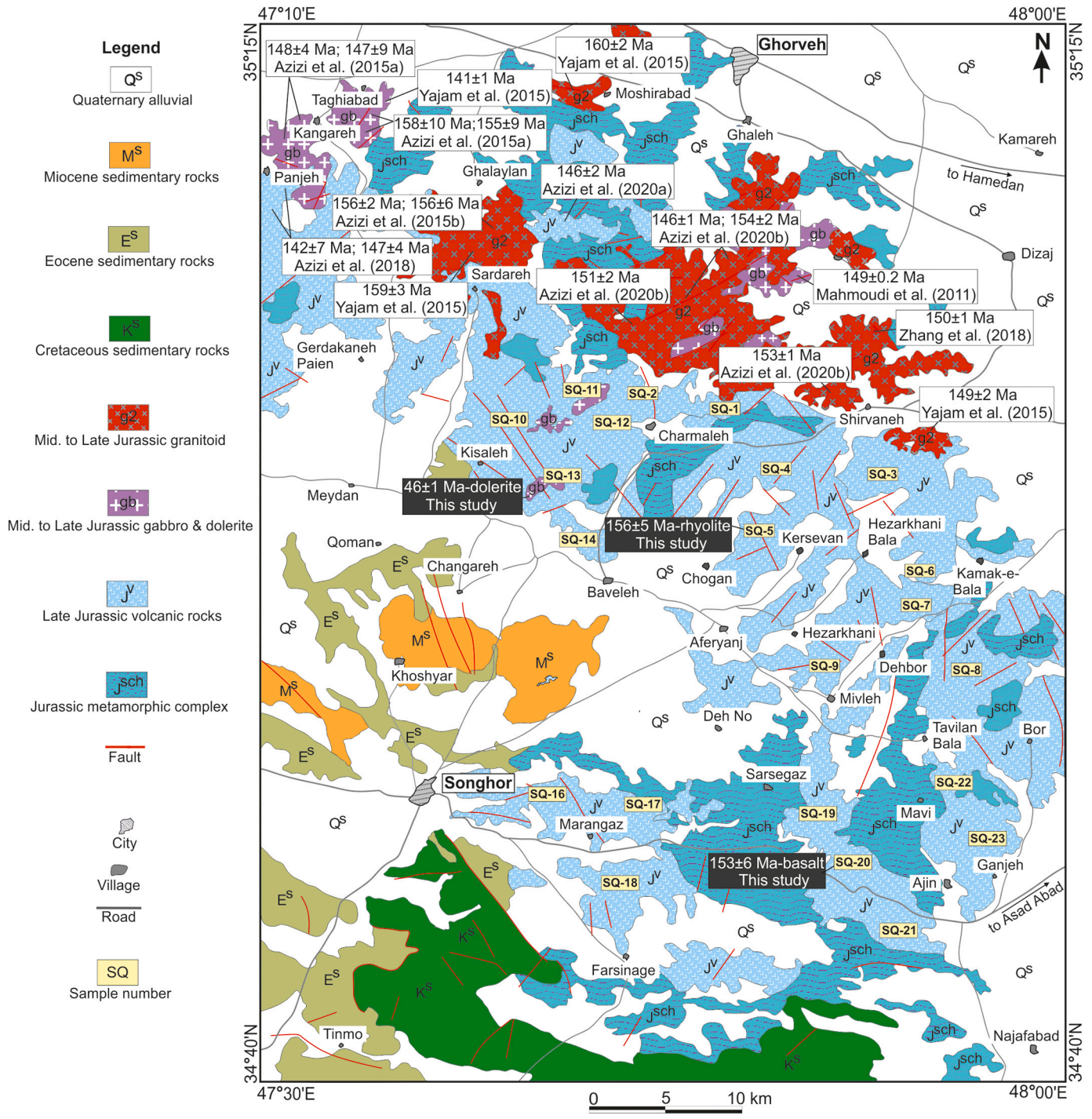

Fig. 2. Simplified geological map of Songhor area, modified from Eshraghi et al. (1996), and sample locations. Volcanic-subvolcanic bodies are surrounded by the Late Triassic to Jurassic sedimentary complex. The main host rocks are the Ghorveh-Songhor metamorphic complex of the Jurassic age.

the province includes the Songhor-Ghorveh metamorphic complex (Azizi and Asahara, 2013) made of slate, phyllite, schist, marble, and quartzite interbedded with submarine metavolcanic rocks. Fossils in SaSZ sedimentary rocks indicate deposition from Late Triassic to Middle Jurassic in a marine setting. Deeper water sedimentary rocks are found to the SW and shallower water sedimentary rocks such as shale and sandstone are found to the NE. These sedimentary rocks experienced contact metamorphism near SaSZ intrusions but farther away primary sedimentary structures are preserved. Jurassic granite is concentrated in the C–SaSZ. In Middle to Late Jurassic times (180–140 Ma), Songhor-Ghorveh basement was intruded by mafic and felsic plutons such as the Mobarak-Abad (Azizi and Asahara, 2013), Ghalaylan (Azizi et al., 2015a) and Kangareh-Taghiabad gabbroic bodies (Azizi et al., 2015b) (Fig. 2). C-SaSZ felsic intrusions include all granite types, mainly I-, and S-types along with minor A-type that have metamorphic aureoles ranging from a few hundred meters to a few kilometers wide.

The strongly magmatic nature of the C-SaSZ contrasts with the less magmatic nature of the S-SaSZ. S-SaSZ basement is mainly Cadomian metamorphic rocks overlain by unmetamorphosed Triassic and Jurassic sediments. Early and Middle Jurassic igneous rocks including calc-alkaline granites have been interpreted as related to Neo-Tethys subduction. In contrast, Hunziker et al. (2015) suggested a continental rift

setting for the 175–170 Ma Jaz-Murian diorite-trondhjemite-plagiogranite complex.

The Songhor complex is situated between the cities of Songhor and Ghorveh in the C-SaSZ (Fig. 2). The local basement comprises the Songhor-Ghorveh metamorphic complex composed of marble, greenschist and amphibolite (Azizi et al., 2015a). Metamorphic basement in the study area was covered by unmetamorphosed Cretaceous sedimentary rocks (Hosseiny, 1999) demonstrating that metamorphism occurred in the Middle to Late Jurassic time (Azizi et al., 2015a; Hosseiny, 1999). The Songhor Early to Mid-Jurassic sequences include volcanic, hypabyssal bodies and volcaniclastics interbedded with marbles, shales, slates, and sandstones. In the study area, the metasediments are mainly foliated marbles, metasandstones, and lesser metapelites interbedded with volcanics.

There are a few detailed studies on the geochemistry, geochronology, and geodynamic setting of Songhor magmatic rocks (Azizi et al., 2020b; Maanijou et al., 2013; Rahimzadeh et al., 2021). Some of these argue that these igneous rocks formed in an arc-back arc system related to an active continental margin in Early Cretaceous time (130–110 Ma: Rahimzadeh et al., 2021). In contrast, Azizi et al. (2020b) infer a rift basin for Jurassic (154–146 Ma) intrusions from the northern Songhor region and do not confirm Cretaceous magmatism. Songhor area lavas interbedded with metasediments can be divided into felsic and mafic groups. The igneous activity started with eruptions of dacitic and rhyolitic lava, grading upwards into basaltic lava interbedded with carbonate rocks (Fig. 3a) and was accompanied by minor felsic dikes and small mafic intrusions (Fig. 2). I and A-type felsic intrusions of quartz diorite, monzonite, diorite, and granodiorite cut the Jurassic metamorphic complex; contact metamorphism overprinted regional metamorphism.

Felsic volcanics are sporadically exposed and comprise rhyolite, trachydacite (Fig. 3b), and hypabyssal micro-diorite. Rhyolite is easily recognizable in the field by abrupt topography and white-to-yellow colors. Micro-diorite is fine-grained and gray to dark green with rough outcrop morphology (Fig. 3c). The mafic group consists of basalt, trachybasalt, and hypabyssal micro-gabbro/dolerite. The basalts are massive to brecciated, dark gray, and porphyritic (Fig. 3d, e). Mafic volcanics (lava, pyroclastics, and pillows; Fig. 3f) are interbedded with sedimentary rocks and locally have been metamorphosed to lower greenschist facies. Black to green dolerite bodies cut host rocks are locally exposed (Fig. 3g, h). Within the complex, small lenses and isolated bodies of felsic igneous rocks and are found in host mafic volcanics (Fig. 3i). The Jurassic igneous complex in the southern and southwest part of the study area is unconformably overlain by Eocene sandstones, marls, and limestones.

3. Analytical techniques

3.1. Zircon U-Pb dating

Three samples were selected for zircon U-Pb age determinations. Two kg of each was crushed, and we used 60–80 mesh sieves to yield this size and smaller fraction. Zircons were separated using a magnetic separator and heavy liquid (bromoform). Separated zircons were examined under a binocular microscope at the University of Kurdistan, Iran. Zircons were mounted in epoxy and the mount was polished using

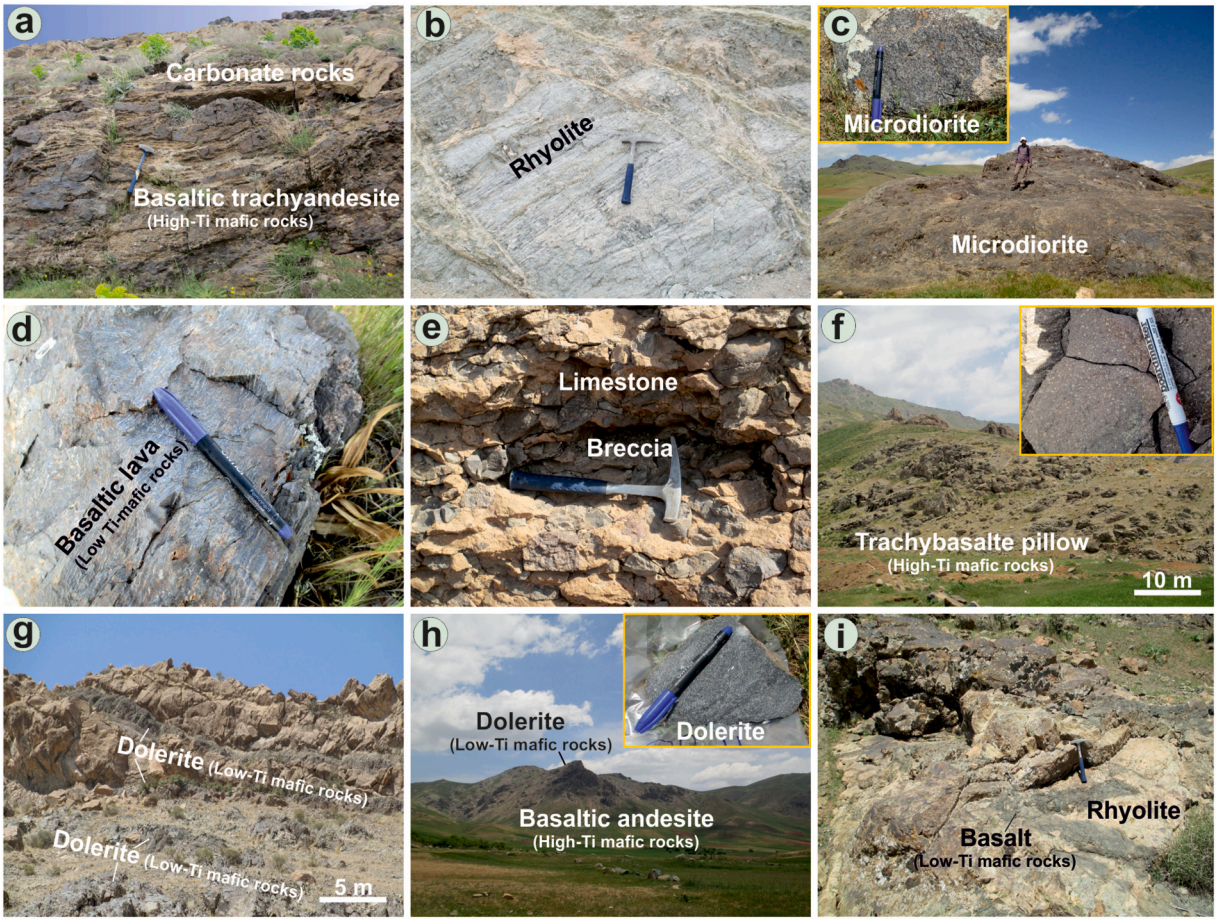

Fig. 3. Photographs of representative outcrops in the study area. **(a)** Limestones interbedded with volcanics. **(b)** Felsic tuffaceous rocks. **(c)** Fine-grained, black to dark microdiorite with rough morphology. **(d, e)** Green and grayish-green basaltic lavas flow and brecciated basalt. **(f)** Pillow lavas and vesicular basalts to andesites. **(g)** Metapelites. **(h)** Fine-grained, black to dark green dolerite with rough morphology. **(i)** Lens, pods and isolated fragments of mafic rocks in silicic lavas.

diamond paste. The mount was photographed in transmitted and reflected light to characterize analyzed grains. Backscattered electron (BSE) and cathodoluminescence (CL) images of the zircons were taken with a scanning electron microscope (HITACHI S-3400 N) equipped with a CL system (GATAN Mini CL) at Nagoya University Museum, Japan. Prismatic crystals with no defects or visible alteration were selected based on the BSE and CL observations. U-Pb data were obtained with a laser ablation (LA, NWR213 Electro Scientific Industries) – inductively coupled plasma mass spectrometer (ICP-MS Agilent 7700×) at Nagoya University, Japan. Detailed descriptions of the LA-ICP-MS analysis procedures are provided in Orihashi et al. (2008). LA spot size was 25 μm. Before measuring zircons, the NIST SRM 610 glass (Pearce et al., 1997) and the 91,500-zircon standard (Wiedenbeck et al., 2004) were analyzed to determine the correction factor for Pb/U fractionation, i.e., the $^{206}Pb/^{238}U$ ratio of the NIST SRM 610 glass normalized by the 91,500-zircon standard (Wiedenbeck et al., 2004). Ablation points for zircons were selected based on the CL and BSE images. In each measurement cycle, eight zircons and one 91,500-zircon standard with eight points for the NIST SRM 610 glass were run. Blank levels were controlled in each cycle. The value of common Pb was estimated using the Stacey and Kramers (1975) model. Zircons with high common Pb ($^{206}Pb_c > 5\%$) were rejected. The mean age of the 91,500-zircon standard (Wiedenbeck et al., 2004) during this study was 1050.1 ± 7.1 Ma ($n = 16$) with a low mean square weighted deviation (MSWD = 0.46). Age calculations, plotting on Concordia, average ages, and histogram diagrams were achieved using the ISOPLOT v.4.15 software.

3.2. Whole rock geochemistry and Sr and Nd isotopes

A 100–200 mg sample of rock powder was decomposed in a covered PTFE (polytetrafluoroethylene) beaker using 3 ml HF (50%) and 0.5–1 ml $HClO_4$ (70%) at 120–140 °C on a hot plate for 72 h. The PTFE cover was then removed, and the decomposed sample was completely dried at 140 °C on a hotplate with infrared lamps for 24–48 h. The dried sample was dissolved in 10 ml of 2.4–6 M HCl and moved to a PE centrifuge tube. After centrifuging the sample solution, the supernatant was moved to the PTFE beaker, and the residue was moved into a small sealed PTFE vessel. After drying the wet residue on a hotplate, 1.5 ml of HF (50%) and 0.5 ml of $HClO_4$ (70%) were added. The small sealed PTFE vessel was set in an outer PTFE vessel, and the outer vessel was inserted into a stainless-steel jacket. The steel-jacketed PTFE bomb was kept in an oven at 180 °C for 3–5 days to completely dissolve any residual minerals. The second decomposed fraction was dried on a hotplate and dissolved in 2.4–6 M HCl. This solution was mixed with the supernatant in the PTFE beaker, and the mixed solution was dried again. The dried sample was dissolved in 10 ml of 2.4 M HCl, and the solution was divided into two aliquots at a ratio of 10:1. The first aliquot (fraction A) was used for natural Sr-Nd isotopes, and the second (fraction B) was used for ICP-MS analysis for trace elements. All aliquots were dried on a hotplate with an infrared lamp. Dried fraction A was dissolved in 3 ml of 2.4 M HCl, and the solution was loaded on a cation exchange column (AG50W-X8, 200–400 mesh) with HCl eluent (2.4 and 6 M). Dried fraction B was dissolved in 2%-HNO_3, and the trace element concentrations were analyzed by inductively coupled plasma mass spectrometry (ICP-MS) (Agilent 7700×) at Nagoya University. The isotope ratios of Sr and Nd were determined by a GVI IsoProbe-T thermal ionization mass spectrometer (TIMS) at Nagoya University. Mass fractionations during measurement were corrected according to $^{86}Sr/^{88}Sr = 0.1194$ and $^{146}Nd/^{144}Nd = 0.7219$. The NISR-SRM 987 and JNdi-1 standards (Tanaka et al., 2000) were used as Sr and Nd isotope ratio standards, respectively. Repeated analysis of NISR-SRM 987 yielded an average $^{87}Sr/^{86}Sr$ of 0.710266 ± 0.000007 ($n = 10$, 1SD), and repeated analysis of JNdi-1 yielded an average $^{143}Nd/^{144}Nd$ of 0.512141 ± 0.000004 ($n = 14$, 1SD).

4. Petrography

4.1. Hypabyssal rocks

These are medium to fine-grained micro-diorite to micro-gabbro and/or dolerite. Micro-diorite contains plagioclase and clinopyroxene (locally replaced by hornblende) as the major rock-forming minerals (Fig. 4a) and microgranular texture is common. Plagioclase is euhedral to subhedral with clear lamellar twinning (Fig. 4a, b). In micro-diorite, clinopyroxene occurs as irregular relicts surrounded by secondary actinolite.

Micro-gabbro/dolerite is dominantly composed of plagioclase, clinopyroxene and olivine showing intergranular and ophitic to subophitic textures (Fig. 4c, d). Plagioclase occurs as euhedral to subhedral tabular grains with lamellar twinning. Olivine is anhedral with curved cracks (Fig. 4d) and is sometimes partly altered to serpentine. Clinopyroxenes form pale green elongated crystals bordering olivine. Magnetite, apatite, and titanite are the main accessories.

4.2. Volcanic rocks

The Songhor volcanic suite is composed of rhyolite to trachydacite and basalt, trachybasalt to basaltic trachyandesite. Rhyolites are porphyritic with quartz, plagioclase, and alkali feldspar phenocrysts (Fig. 4e, f). Quartz, alkali feldspar, and plagioclase are commonly subhedral and embayed around margins (Fig. 4f). Trachydacite shows trachytic and pyroclastic to flow textures, containing amphibole and plagioclase (Fig. 4g). Basalts and trachybasalts display porphyritic and intersertal textures (Fig. 4h). The major constituents of these rocks are plagioclase, pyroxene, and amphibole with magnetite and titanite as accessory minerals (Fig. 4i). The matrix comprises elongated plagioclase with subordinate titanite and Fe-Ti oxides. Some plagioclase phenocrysts are replaced by epidote and albite.

5. Results

5.1. Zircon U-Pb age dating

The LA-ICP-MS U-Pb Concordia diagrams and cathodoluminescence (CL) images of Songhor rhyolite (SQ-5), trachybasalt (SQ-13), and dolerite (SQ-18) are shown in Figs. 5 and 6. The zircon LA-ICP-MS U-Pb dating results are listed in Table S1.

5.1.1. Rhyolite

Zircons from sample SQ-5 are euhedral and prismatic, and transparent to colorless, measuring 50 to 300 μm long (Fig. 5a). Most zircons have weak oscillatory zoning and Th/U ratios of 0.34–0.75 with a mean of 0.60, suggesting their crystallization from the melt. Twenty-four spots were ablated. Fourteen spots yielded concordant $^{206}Pb/^{238}U$ ages from 154 Ma to 137 Ma with a mean $^{206}Pb/^{238}U$ age of 156.5 ± 5.5 Ma (MSWD = 0.70, $n = 14$; Fig. 6a-b).

5.1.2. Basaltic andesite

Zircons from sample SQ-13 are transparent and subhedral to euhedral (Fig. 5b). They have lengths of 80 to 150 μm. Most zircons show gray luminescence and obvious oscillatory zoning and have high Th/U ratios of 0.59 to 3.97 with a mean of 1.27, indicative of igneous derivation. Fifteen concordant analyses yielded $^{206}Pb/^{238}U$ ages ranging from 163 Ma to 141 Ma with a mean of 153.3 ± 3.3 Ma (MSWD = 0.9, $n = 15$; Fig. 6c-d), interpreted as the crystallization age of the basalt.

5.1.3. Dolerite

Zircons from dolerite (SQ-18) are light purple to transparent, with long to short prismatic shapes (Fig. 5c). CL images reveal that these zircons have clear oscillatory zoning with high Th/U ratios of 0.44 to 2.41 with a mean of 1.40, typical of magmatic zircons. A total of 25 spots

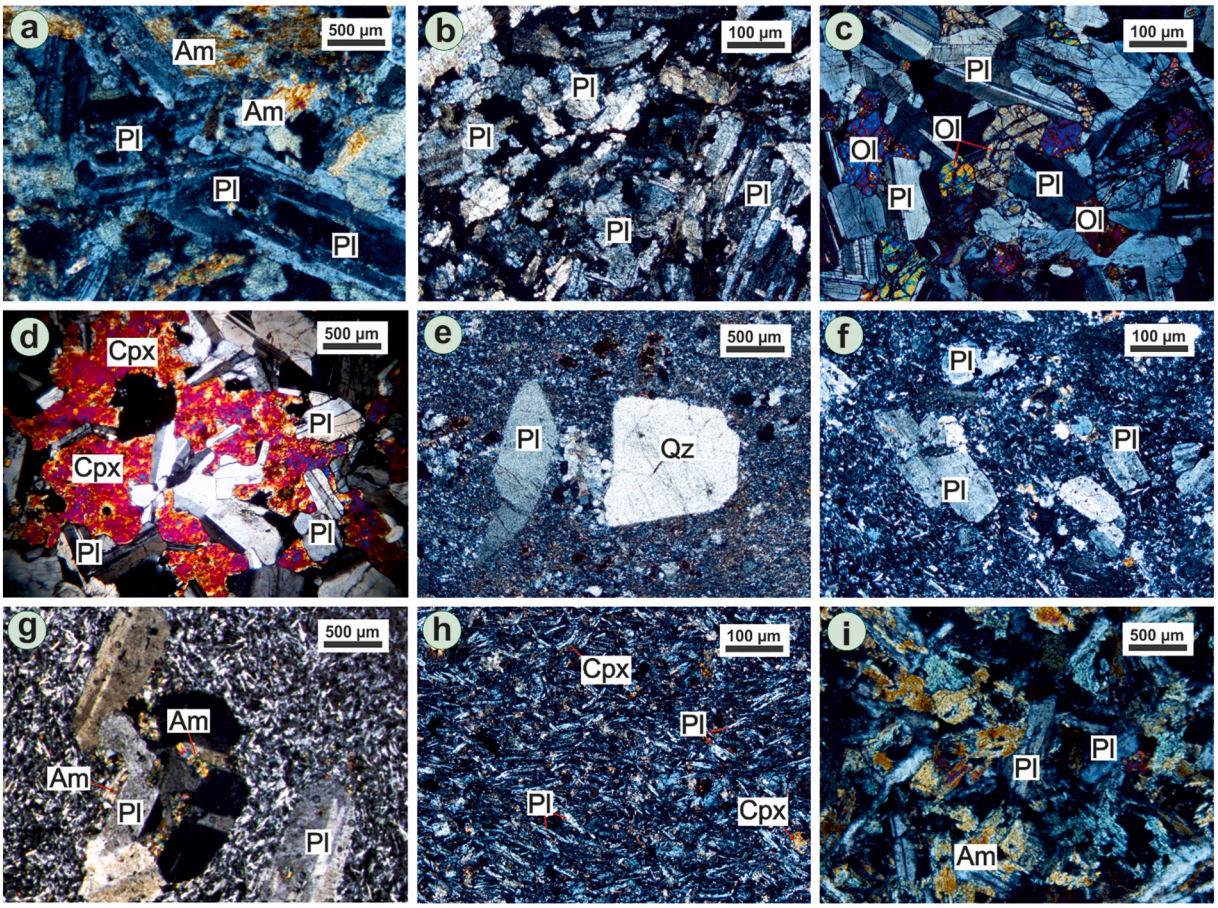

Fig. 4. Photomicrographs of Songhor magmatic rocks. **(a)** Micro-diorite with hornblende and plagioclase as major rock-forming minerals. **(b)** Euhedral to subhedral plagioclase in basalt with clear lamellar twinning. **(c, d)** Micro-gabbro is dominated by plagioclase, clinopyroxene, and olivine with ophitic and sub-ophitic textures. **(e, f)** Porphyritic rhyolite and dacite with abundant quartz and plagioclase phenocrysts. **(g)** Andesite containing amphibole, plagioclase. **(h, i)** Basalt with intersertal texture. Major constituents are plagioclase, amphibole and pyroxene. Hbl= Hornblende, Qz= Quartz, Pl= Plagioclase, Cpx= Clinopyroxene, Ol= Olivine.

were analyzed, of which ten spots were concordant and yielded a mean $^{206}Pb/^{238}U$ age of 146.4 ± 1.0 Ma (MSWD = 0.96, n = 10; Fig. 6d-e). Taking error estimates into consideration, the zircon U-Pb ages indicate that all magmatic rock types were emplaced between 156 and 146 Ma in the Late Jurassic time.

5.2. Bulk rock chemistry

The results of major and trace element analyses for 24 Songhor complex volcanic and hypabyssal rocks are given in Table S2. The loss on ignition (LOI) for most samples is <3 wt%, indicating modest alteration. Volcanic to hypabyssal rocks of the Songhor area range from mafic to felsic, although intermediate rock types are rare. Data are graphically compared to volcanic to plutonic rocks from the Songhor and Ghorveh areas.

Total alkali versus silica (TAS) classification diagram (Middlemost, 1994) shows that most felsic rocks are trachydacite and rhyolite (Fig. 7a). Felsic samples contain 62.6 to 73.9 wt% SiO_2, 2.6 to 5.9 wt% Na_2O, 2.5 to 4.8 wt% K_2O and 0.3 to 1.2 wt% TiO_2. Most felsic rocks have high total alkalis ($K_2O + Na_2O$ = 5.1–9.8 wt%) and plot in the calc-alkaline to high-K calc-alkaline (Fig. 7b: Peccerillo and Taylor, 1976) and metaluminous to peraluminous fields (Fig. 7c). Contents of TiO_2, MnO, Fe_2O_3, CaO, P_2O_5 and MgO decrease with increasing silica, along with increasing K_2O contents and little variation for Al_2O_3 (Fig. 8).

On chondrite-normalized REE (Sun and McDonough, 1989) diagrams, felsic rocks are enriched in LREE, with significantly negative Eu anomalies (Fig. 9a), similar to the composition of bulk continental crust (BCC) (Rudnick et al., 2003) and crust-derived granites (Tao et al., 2014). The rather flat HREE patterns imply the absence of garnet and/or hornblende in the source of these magmas and the strong negative Eu anomalies indicate an important role for feldspar; together these features are most consistent with low-pressure melt formation and fractionation. These rocks also exhibit positive anomalies for large ion lithophile elements (LILIEs) such as Cs, Rb, Th, U and Pb with some negative anomalies for Nb, Ta, Ti, Sr, and Zr (Fig. 9b).

All mafic samples plot in the basalt, trachybasalt, or basaltic trachyandesite fields (Fig. 7a) (Middlemost, 1994). Seven samples plot in the sub-alkaline and 8 plot in the alkaline field (Fig. 7a). Songhor mafic rocks can be divided into two groups (Fig. 7d): high-Ti series showing nearly constant TiO_2 and low-Ti series showing a steep trend of variable TiO_2 (Fig. 7d). Sub-alkaline mafic rocks (3 basalts and 4 micro-gabbro/dolerites) belong to the low Ti group and plot in the tholeiitic to calc-alkaline fields in the SiO_2 versus K_2O variation diagram (Fig. 7b: Peccerillo and Taylor, 1976). These have low SiO_2 (47.0–49.8 wt%), moderate Fe_2O_3 (7.4–10.7 wt%), and unusually low TiO_2 (0.1–0.6 wt%) and high MgO (7.1–10.7 wt%) and Al_2O_3 (17.7–20.0 wt%) abundances. The samples define steeply decreasing abundances of Fe_2O_3, MnO, CaO, and MgO with increasing SiO_2 contents.

Alkaline mafic rocks belong to the high-Ti series and plot in the calc-alkaline to alkaline fields in the SiO_2 versus K_2O diagram (Fig. 7b: Peccerillo and Taylor, 1976). The samples show narrow compositional variations with higher SiO_2 (50.8–54.7 wt%) and TiO_2 (1.4–1.6 wt%) and lower MgO (4.1–8.4 wt%). Harker diagrams (Fig. 8) show nearly constant values for TiO_2 and Al_2O_3 with increasing SiO_2 content,

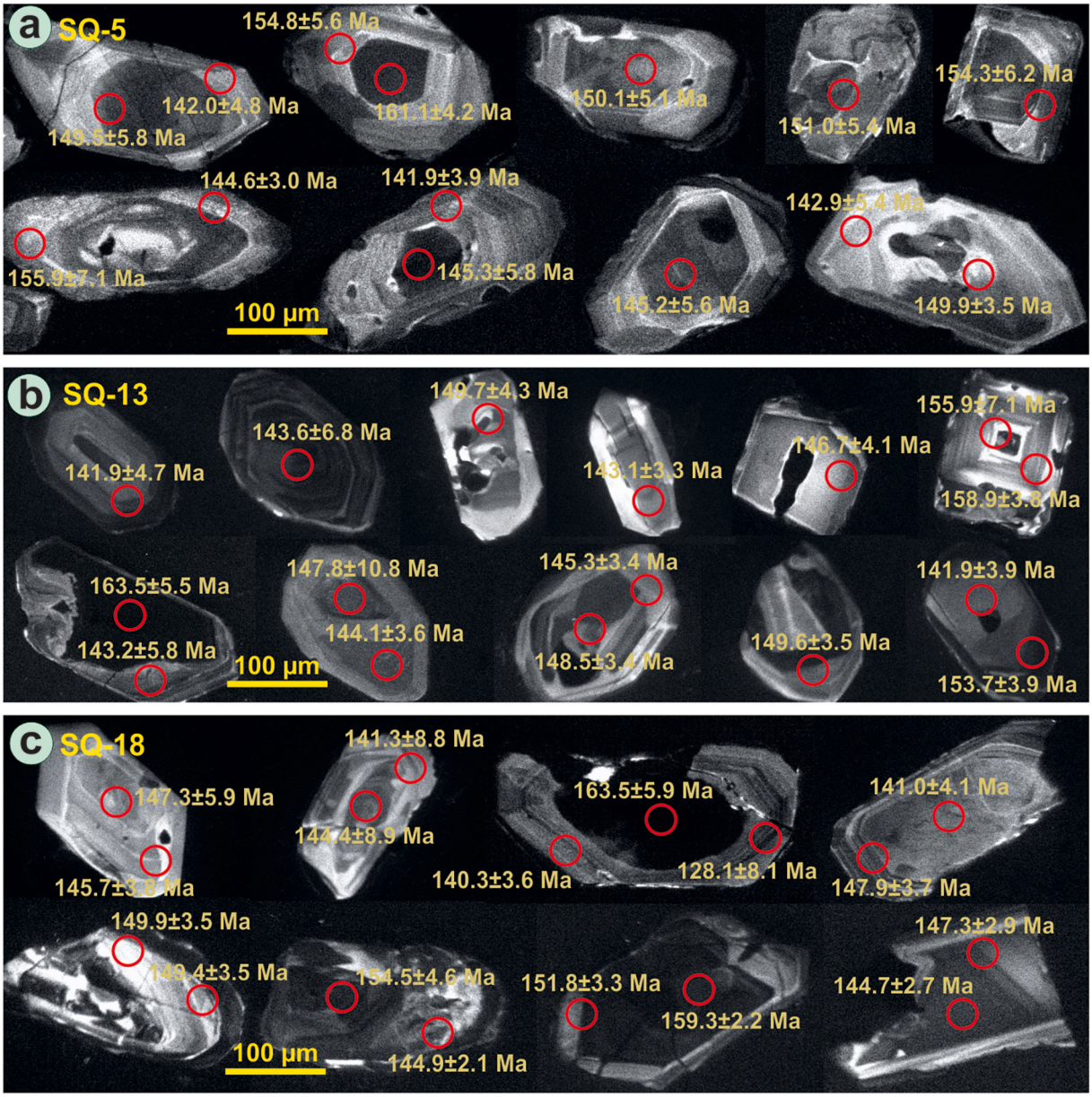

Fig. 5. (a-c) Cathodoluminescence (CL) images of some zircons from Songhor magmatic rocks (SQ-5, SQ-13, and SQ-18). Some of the analyzed spots on zircon grains with ages are shown.

decreasing MgO, Fe_2O_3, and CaO, and increasing P_2O_5 and alkalis.

Mafic low-Ti series show affinities with MORB and tholeiites, whereas high-Ti series are alkaline and OIB-like. Their chondrite normalized REE patterns (Sun and McDonough, 1989) range from flat to LRE*E*-enriched (Fig. 7c). Total REE contents for the high-Ti series (53.6–174 ppm) are higher than those for the low-Ti series (9.5–45.0 ppm). REEs in the low-Ti series behave differently for basalts and micro-gabbro/dolerites. Low-Ti basalts show flat REE patterns and lack Eu anomalies (Fig. 9c). Low-Ti micro-gabbro/dolerites have very low REE contents (9.5 to 11.2 ppm), with high LREE/HREE ratios and positive Eu anomalies suggesting plagioclase accumulation; this is consistent with high Al_2O_3 and CaO contents (Fig. 8). In contrast, the high-Ti series is LREE-enriched with La/Yb ratios ranging from 2.4 to 7.5 (Fig. 9c), midway between OIB and E-MORB. On the primitive mantle normalized diagram, strong depletions of Nb and Ta and enrichments in Pb, Eu, and Sr are observed in the low-Ti doleirtes (Fig. 9d). In contrast, the high-Ti series is less depleted in HFSEs such as Nb and Ta relative to other incompatible elements.

5.3. *Whole rock Sr-Nd isotope ratios*

Sr and Nd isotope ratios of the samples are listed in Table S3. The initial values of $^{87}Sr/^{86}Sr$ and $^{143}Nd/^{144}Nd$ were calculated for 156 and 146 Ma based on U-Pb zircon ages from felsic and mafic rocks, respectively. Initial $^{87}Sr/^{86}Sr$ ratios of felsic rocks range from 0.7041 to 0.7062 (filtered to exclude samples with $^{87}Rb/^{86}Sr > 4$, and sample SQ-19 with $^{87}Sr/^{86}Sr = 0.7117$, possibly due to remobilization of Rb during alteration. They have initial $^{143}Nd/^{144}Nd$ ratios from 0.51248 to 0.51264, with εNd(t) values of +0.6 to +3.8, except sample SQ-19 with εNd(t) = −6.7.

Low-Ti mafic rocks have similar $^{143}Nd/^{144}Nd(i)$ ratios of 0.51261–0.51274 with εNd(t) values +3.2 to +5.8, but slightly lower $^{87}Sr/^{86}Sr(i)$ ratios of 0.7032 to 0.7033 for low-Ti micro-gabbros/dolerites than low-Ti basalts (0.7053–0.7059). High-Ti mafic rocks have broadly similar $^{87}Sr/^{86}Sr(i)$ and lower $^{143}Nd/^{144}Nd(i)$ ratios ranging from 0.7039 to 0.7056 and 0.51251 to 0.51266, with εNd(t) values +1.2 to +4.2 (Table S3).

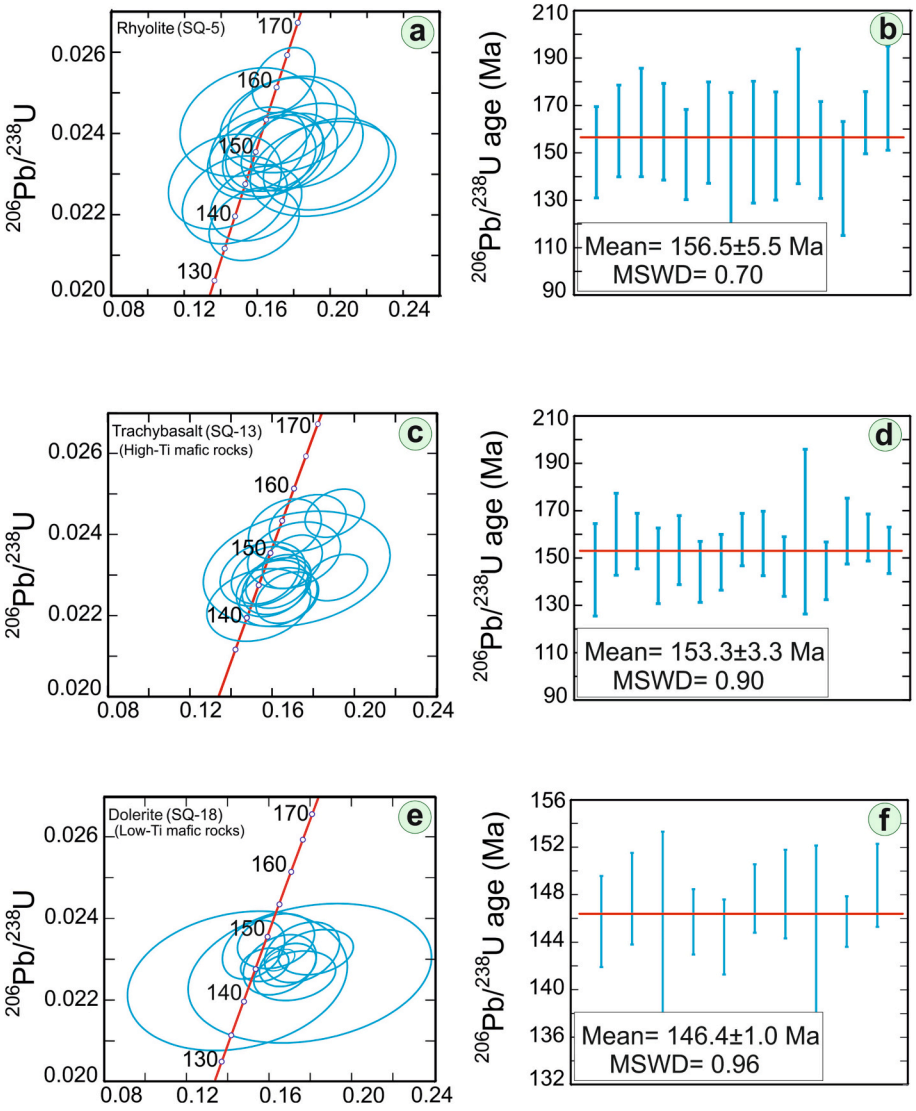

Fig. 6. U-Pb Concordia diagrams and ^{238}U–^{206}Pb age distribution diagrams for zircons obtained from **(a, b)** rhyolite (SQ-5), **(c, d)** trachybasalt (SQ-13), and **(e, f)** Dolerite (SQ-18). None of the three samples have any inherited zircons and show similar U-Pb ages.

The εNd(t) and $^{87}Sr/^{86}Sr(i)$ values for Songhor magmatic rocks are shown in Fig. 10a together with fields for MORB and oceanic island basalts (OIB), as well as fields for igneous rocks from the Okinawa Trough, Siberian high and low-Ti flood basalts, Afar (Castillo et al., 2020), Tarim (Qin et al., 2011), and Emeishan (Anh et al., 2011; Zhu et al., 2021) CFBs and LIPs. Songhor mafic rocks display a relatively narrow range of εNd(t) and $^{87}Sr/^{86}Sr(i)$, plotting below the MORB field and within the OIB fields along with several famous LIPs such as Afar and Emeishan. The felsic rocks overlap with the field of the mafic rocks, but generally show lower εNd(t) and higher $^{87}Sr/^{86}Sr(i)$ values.

Nd model ages (T_{DM1}) for Songhor rocks are 712 to 1027 Ma (Table S3). This data set (T_{DM1}) was filtered to exclude samples with $^{147}Sm/^{144}Nd > 0.165$, considered to yield unreliable model ages (Stern, 2002), because the rocks with high $^{147}Sm/^{144}Nd$ will intercept the depleted mantle growth curve very obliquely. The mafic rock samples with flatter REE patterns show older Nd model ages.

6. Discussion

Here, we use our new data to address three related questions: 1) how did Songhor felsic magmas form? 2) how did Songhor mafic magmas form? and 3) what tectonic environment did these magmas form in and what is their significance for understanding the Jurassic tectonic setting of the SaSZ?

6.1. Petrogenesis of felsic rocks

Songhor bimodal mafic-felsic suites are compositionally similar to many bimodal suites worldwide. Such bimodal suites include those from both large igneous provinces such as the Panjal traps of India (Shellnutt et al., 2012), Tieshajie group of S-China (Li et al., 2013), Haida Gwaii of Canada and some volcanic complexes of northern New Brunswick of Canada (Dostal et al., 2021). Studies reveal that the felsic end–member of the bimodal magmatism in different tectonic settings can have distinct geochemical characteristics (Natali et al., 2011). For instance, the felsic end–member is usually similar to A–type/ferroan granites when bimodal magmatism happens in an intraplate setting (Turner and Rushmer, 2009), whereas in arc settings, it shares similarities to S– or I–type granites. Songhor felsic rocks show high $10^4 \times$ Ga/Al ratios (3.01–4.05), Nb + Y contents (> 60), K_2O + Na_2O contents (8.23–9.51%), and Zr + Nb + Ce + Y contents (289–624 ppm) and mostly plot in the A-type field in various discrimination diagrams (Fig. 11a- d; Whalen et al., 1987; Whalen and Hildebrand, 2019).

Large compositional variations have been found for A-type felsic

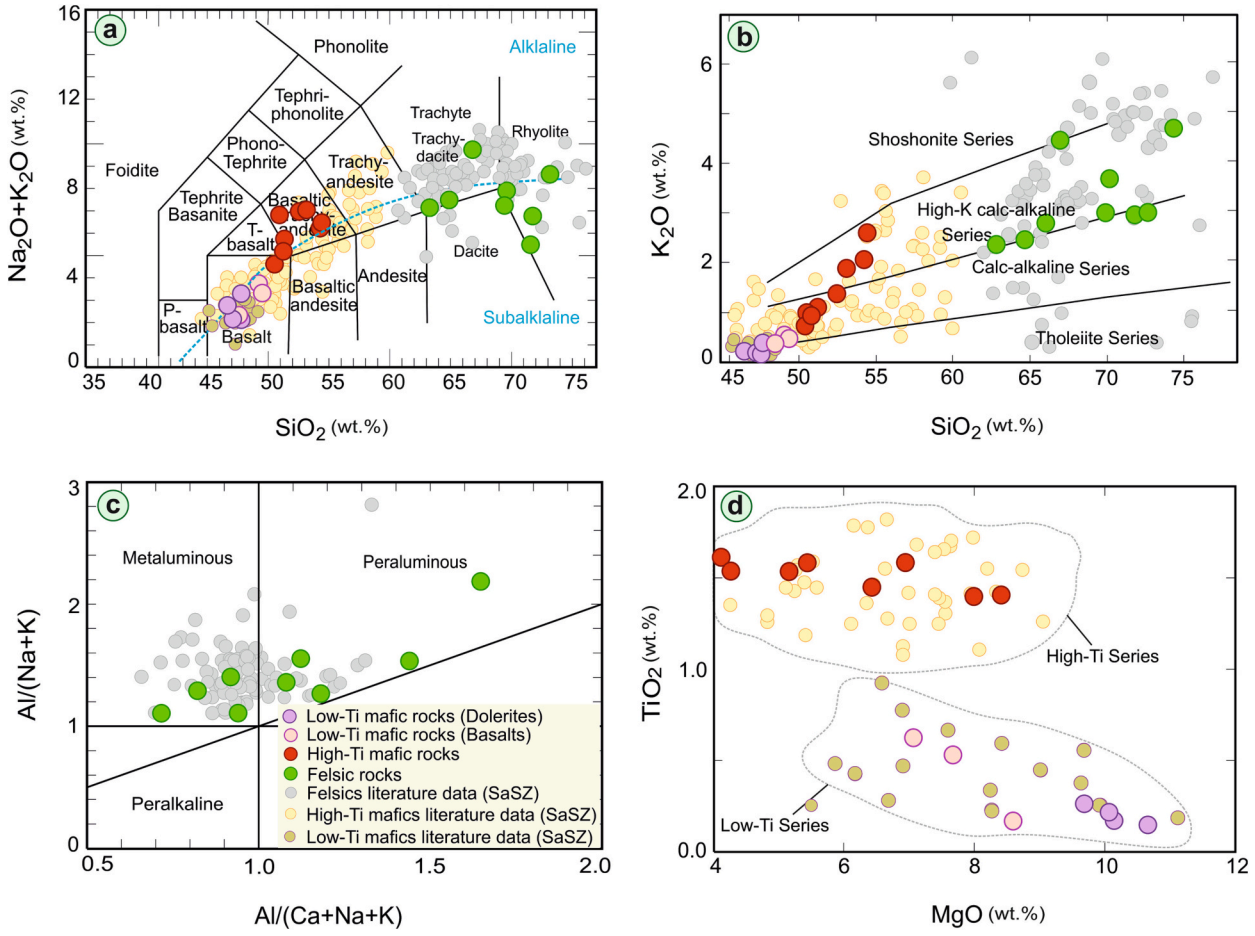

Fig. 7. Chemical classification diagrams for the Songhor magmatic rocks. **(a)** Rock classification diagram of SiO_2 versus Na_2O+K_2O (Middlemost, 1994). **(b)** K_2O–SiO_2 (wt.%) variation diagram (Peccerillo and Taylor, 1976). **(c)** The plot of A/CNK [$Al_2O_3/(CaO+Na_2O+K_2O)$] versus A/NK [$Al_2O_3/(Na_2O+K_2O)$]. **(d)** MgO versus TiO_2 variation diagram. Data for magmatic rocks from Mahmoudi et al. (2011); Maanijou et al. (2013); Azizi and Asahara (2013); Azizi et al. (2011, 2015a,b, 2018, 2020a,b); Yajam et al. (2015); Tavakoli et al. (2021) and C-SaSZ rocks from Azizi and Stern (2019) and references therein are also shown for comparison.

rocks, and there is no consensus on their origin. A-type felsic rocks are genetically diverse and can be produced from various sources and by different processes. There are three possible mechanisms for the generation of the felsic rocks: (1) mixing between mantle- and crust-derived magmas, (2) fractional crystallization of mantle-derived basaltic magmas (Barth et al., 1995) and (3) partial melting of crustal material either the upper crust or earlier underplated mafic lower crust (Brewer et al., 2004).

Mixing between mantle- and crustal-derived melts has been proposed to produce A-type felsic rocks, which generally have a wide range of elemental and isotopic compositions. However, our samples show narrow ranges. Also, mafic microgranular enclaves, representing magma mixing are absent.

One process that is commonly invoked for the genesis of felsic magmas is the extensive fractional crystallization of mantle-derived basaltic magma. Felsic rocks formed by fractional crystallization are usually associated with mafic to intermediate rocks, which are missing from the Songhor area. There is a large SiO_2 gap (Daly gap) between Songhor mafic and felsic igneous rocks (Fig. 8). It is possible (but unlikely) that intermediate rocks were undersampled, but we don't think so. Some argue that the Daly gap may result from massive oxide crystallization (Shellnutt et al., 2009). The scarcity of intermediate rocks is often taken to indicate that felsic magmas do not form by fractional crystallization of mafic magma (Dostal et al., 2021). In addition, the volume of parental basaltic melts required for ~70–80% fractional crystallization is ~2.5–5 times higher than the proportion of felsic magma erupted (Dostal et al., 2021). Extensive fractional crystallization to form felsic magmas is not favored by what we have learned about the geology of the Songhor area (this study; Maanijou et al., 2013). Thus, the question remains regarding how large volumes of C-SaSZ felsic magmas were produced.

Another possible mechanism is the partial melting of the crust. A diversity of crustal protoliths has been proposed in various crust partial melting models for the origin of A-type (like) felsic rocks, including (1) metasedimentary rocks under high temperature; (2) anhydrous lower crustal granulitic residues from which a granitic melt was previously extracted (Whalen et al., 1987); and (3) partial melting of mafic lower crust emplaced during earlier magmatism.

Melting of metasedimentary rocks is not a convincing petrogenetic model for the Songhor felsic rocks because these have lower initial $^{87}Sr/^{86}Sr$ ratios (0.7041 to 0.7062) than A-type granites from other regions derived from metasedimentary rocks- (> 0.715). Melting of metasediments usually produce magmas with strongly peraluminous character. The highly alkaline and low Al_2O_3 contents of all Songhor felsic rocks, along with their metaluminous to weakly peraluminous natures, are incompatible with an origin by melting metasediments. Additionally, partial melting of a refractory granulitic residue that was previously depleted to make hydrous felsic melt would produce felsic magma that was depleted in alkalis relative to alumina, and in TiO_2 relative to MgO (e.g., Patiño Douce, 1997). However, Songhor felsic rocks are characterized by high $(Na_2O + K_2O)/Al_2O_3$ (> 1.0) and TiO_2/MgO (> 1.0) ratios inconsistent with a residual granulite origin.

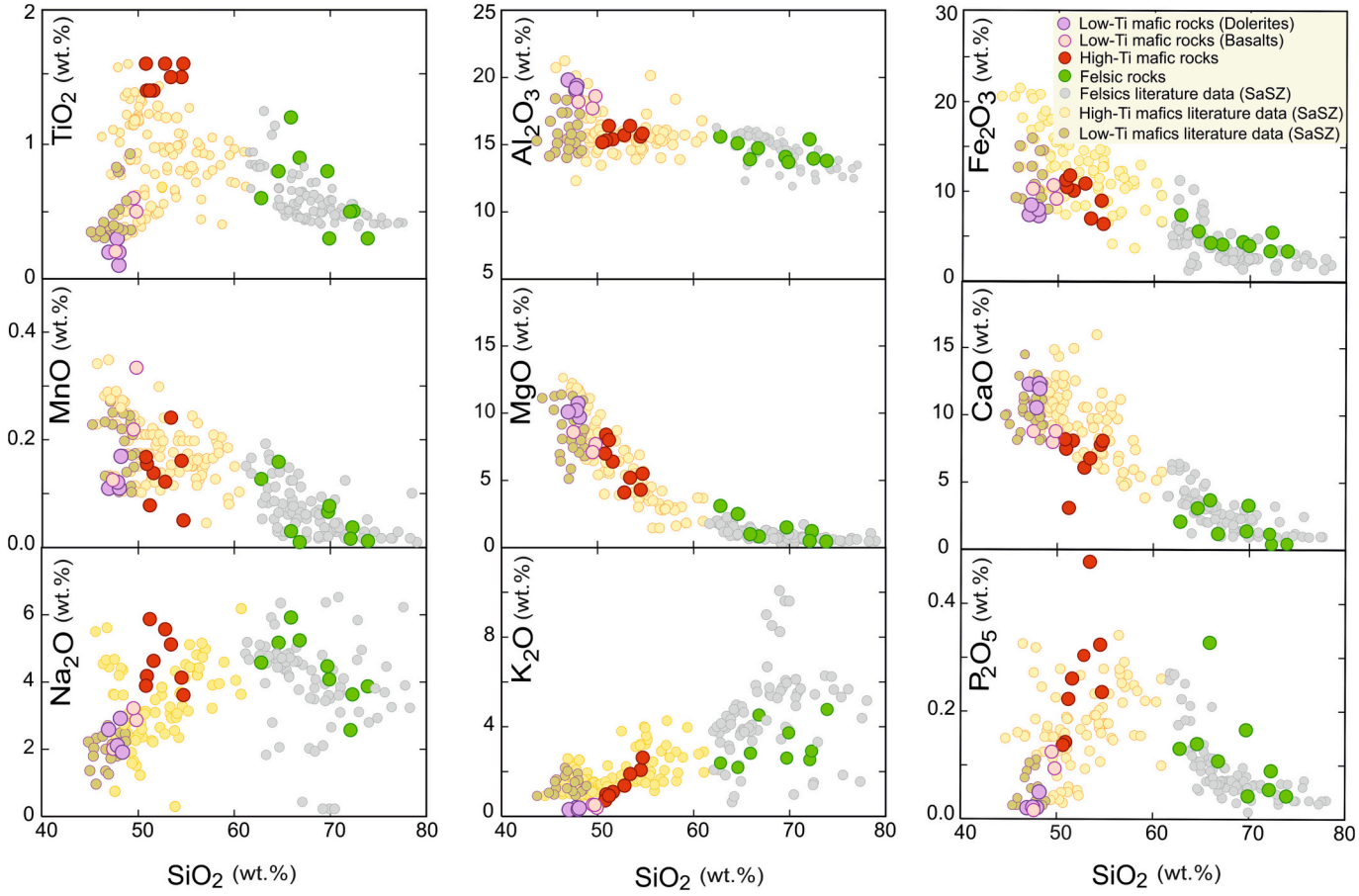

Fig. 8. Major element Harker diagrams for Songhor and nearby Jurassic magmatic complexes. For felsic samples, trends for TiO_2, MnO, Fe_2O_3, CaO, P_2O_5, and MgO contents decrease with increasing silica whereas K_2O contents increase and nearly horizontal variations are observed for Al_2O_3. The mafic samples show steep trends for TiO_2, Fe_2O_3, MnO, and Na_2O with increasing SiO_2 content (wt.%); Al_2O_3, MgO and CaO decrease and K_2O and P_2O_5 increase with increasing SiO_2 content.

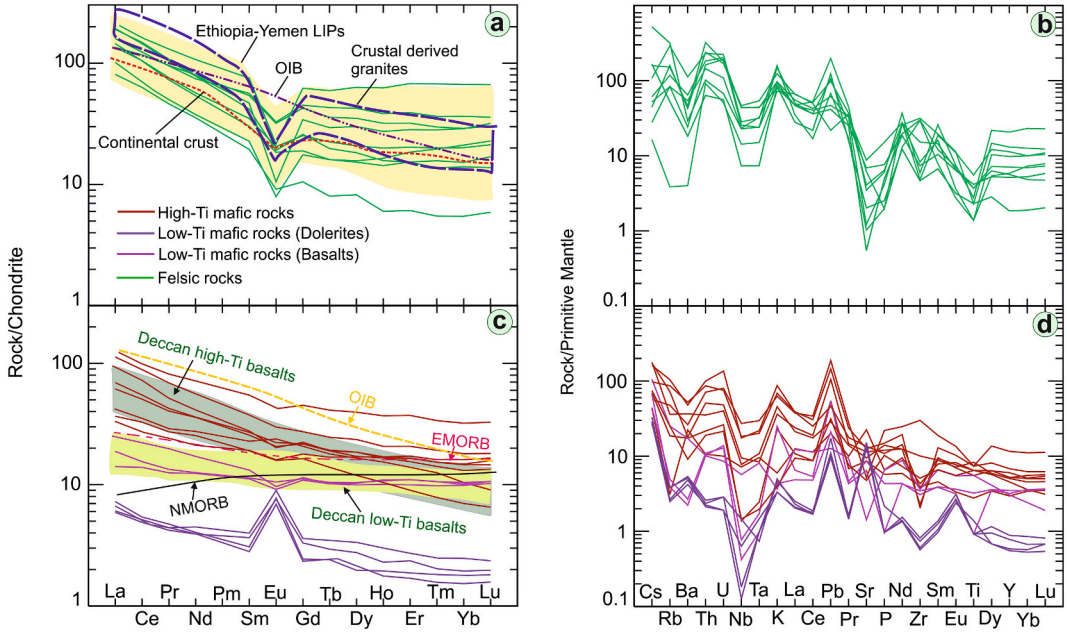

Fig. 9. (a-d) Chondrite-normalized rare earth element and primitive mantle normalized trace element patterns. Data for OIB, NMORB, and EMORB from Sun and McDonough (1989), for continental crust from Rudnick et al. (2003), and for Ethiopia-Yemen from Corti (2009). Data for Deccan high- and low-Ti basalts are from Melluso et al. (2006), and crust-derived granites from Tao et al. (2014).

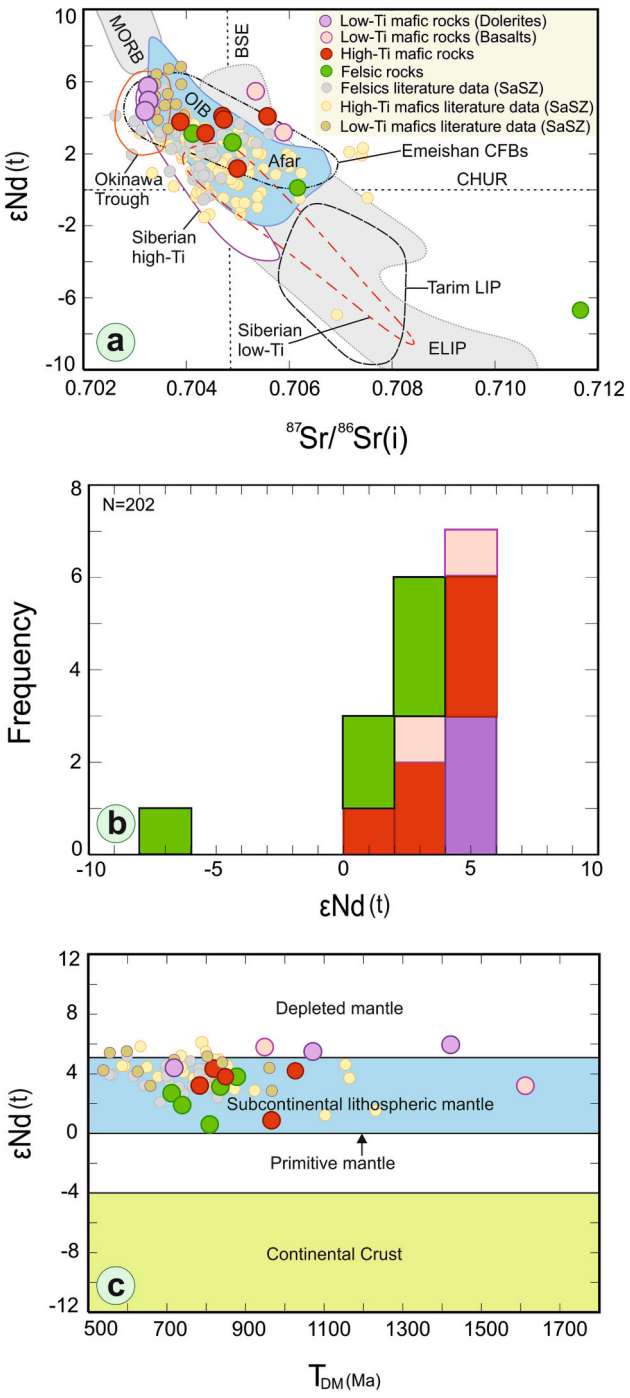

Fig. 10. (a) $^{87}Sr/^{86}Sr(i)$ versus εNd(t) diagram. Most of the Songhor mafic rocks display a narrow range of $^{87}Sr/^{86}Sr(i)$ ratios at the lower end of the MORB field and within the fields of OIB and continental flood basalts, while microgabbros and/or dolerites fall in the field between OIB and Okinawa Trough (Shinjo et al., 1999 and references therein). The isotopic compositions of felsic rocks overlap the mafic rock field. Fields are also shown for Okinawa Trough and Afar, Tarim, and Emeishan CFBs and LIPs (Castillo et al., 2020; Qin et al., 2011; Anh et al., 2011; Zhu et al., 2021). Also shown are separate fields for low-Ti and high-Ti basalts from the Siberian CFB (Sharma et al., 1992). Emeishan large igneous province (ELIP). **(b)** εNd(t) histogram for Songhor igneous rocks, showing the bimodal nature of the igneous activity. Showing overlapping the isotopic composition of felsic and mafic rocks with some crustal interaction for felsic type. **(c)** Coupled variations of T_{DM} versus εNd(t) suggest that Songhor magmas were derived from partial melting of the subcontinental lithospheric mantle of mostly Neoproterozoic age.

Furthermore, the depletion in Ca and Al and enrichment in K and Si of these A-type felsic rocks do not match with those of such a residual origin that should be enriched in Ca and Al and depleted in K and Si.

The partial melting of mafic lower crust may be a suitable mechanism to yield Songhor felsic magmas (Mahoney et al., 2008; Thy et al., 1990). Experiments reveal that dehydration melting of mafic rocks such as amphibolites in the lower crust can generate a felsic melt with high K content (Fig. 11e) (e.g., Thy et al., 1990; Tian et al., 2018). Brophy (2008) recognized that partial melting of amphibole-bearing crust produces distinct REE patterns, which can distinguish between partial melting and fractional crystallization processes. The high Al_2O_3 contents of Songhor felsic rocks and its decrease with increasing SiO_2 (Fig. 8) is similar to experimental basaltic melts of Thy et al. (1990), consistent with the partial melting of a mafic parent. Brophy (2008) recognized that creating felsic melts from partial melting of the mafic lower crust due to magmatic differentiation results in correlated SiO_2 and REE concentrations. In contrast, dehydration melting of amphibolite produces a negative correlation between SiO_2 and REE concentrations (Brophy, 2008). The decrease of REE concentrations with SiO_2 (not shown) for Songhor felsic rocks is consistent with amphibolite melting.

Felsic rocks have slightly positive εNd(t) = +0.6 to +3.8 (average = +2.4, excepting one sample with −6.7), overlapping the isotopic composition of mafic rocks (εNd(t) = +1.2 to +5.8; average = +4.1). This is consistent with the idea that remelting underplate basaltic lower crust generated felsic magmas. As the high SiO_2 and very low MgO contents of the felsic rocks indicate that these could not be generated by direct partial melting of a mantle source, we propose that felsic magma was most likely produced by partial melting of the mafic rocks in the lower crust. The generation of A-type magma requires high temperature, which can be caused by mantle upwelling or mantle-derived mafic magma influx (Dostal et al., 2021).

The question remains why the studied rocks have isotopic and chemical characteristics of OIB rather than depleted MORB. Stein and Hofmann (1992) and Ma et al. (2014) suggest that mantle plumes rarely lead to progressive, oceanic-type hotspot volcanism when they encounter stable subcontinental lithosphere. Clear surface expression of a mantle plume occurs only in rare cases, namely when a plume is exceptionally strong, as seems to be the case for the Yellowstone plume (e.g., Schmandt et al., 2012). Weaker plumes will "underplate" the subcontinental lithosphere or crust with relatively enriched, plume-like mantle material. This material is normally tapped by volcanism only when rifting occurs. It implies that plume material will have accumulated and spread out at the base of this region, possibly over the course of hundreds of millions of years. This underplated material will then be the first to undergo partial melting when the lithosphere is destabilized by rifting. The lithospheric mantle beneath Iran may be the ultimate source of moderately depleted εNd(t) values of the Songhor felsic rocks as this would be preserved in mafic rocks remelted to make felsic magmas. Remelting of underplated mafic magmas could also produce melts that mix with minor Cadomian crustal melts (Supplementary Fig. 1a, b) to yield felsic magmas with the observed isotopic signatures (Mahmoudi et al., 2011). Lithospheric delamination or extension may have permitted slightly depleted lithospheric mantle melts to be injected into the crust with the addition of continental materials, followed by remelting to produce Songhor felsic rocks. The existence of some samples such as SQ-19 with very high $^{87}Sr/^{86}Sr(i)$ (= 0.7117) and negative εNd(t) = −6.8 and samples with low Mg# (< 40) support the idea of localized Cadomian basement partial melting.

6.2. *Petrogenesis of mafic rocks*

Songhor mafic rocks display calc-alkaline to alkaline (high-Ti suite) and calc-alkaline to tholeiitic (low-Ti suite) affinities. High-Ti and low-Ti mafic rocks are easily distinguished by a TiO_2 gap (Fig. 8). The low-Ti suite is less fractionated, with Mg# between 56 and 74 compared to 43 to 63 for high-Ti basaltic rocks. The less fractionated nature of the low-Ti

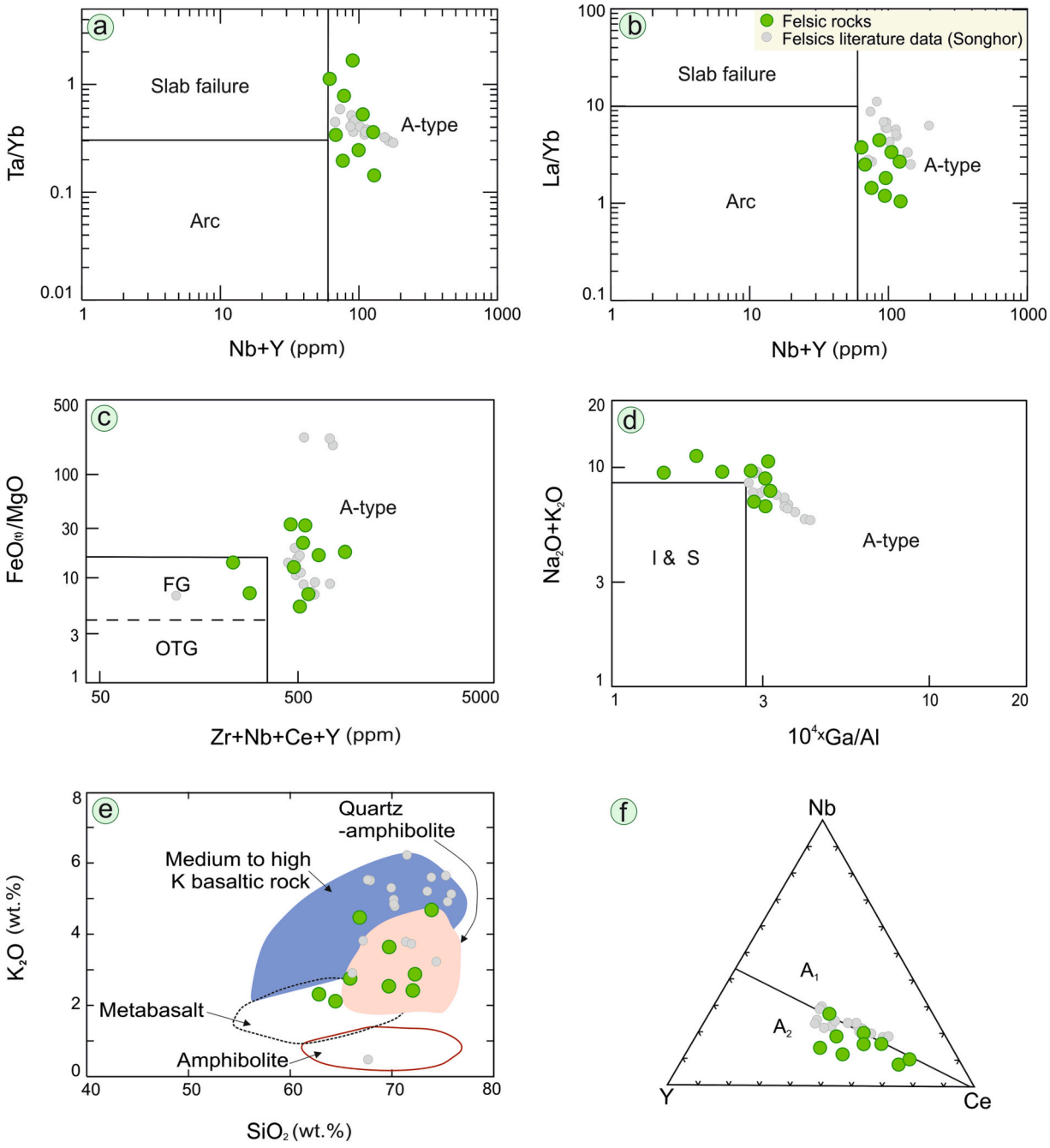

Fig. 11. **(a, b)** Ta/Yb vs. Nb + Y (ppm) and La/Yb vs. Nb + Y (ppm) discrimination diagrams of Whalen and Hildebrand (2019) showing the A-type characteristics of the felsic rocks. **(c, d)** (Zr + Nb + Ce + Y) vs. (FeO/MgO and Ga/Al×10^4 vs. Na_2O+K_2O diagrams distinguishing A-type and I/S-type granites (Whalen et al., 1987). **(e)** wt.% SiO_2 versus K_2O diagram with published data for experimental melts as compiled from the literature: (amphibolites; 1, 3, 6, 9 kb; 800–1000 ∘C), Rapp and Watson (1995) (metabasalts; 8–32 kb; 1000–1125 ∘C), Patiño Douce and Beard (1995) (quartz amphibolites; 3–15 kb; 850–930 ∘C); Patiño Douce and Beard (1995) (medium to high K basaltic rocks; 700 Mpa; 825–975 ∘C). **(f)** Nb–Y–Ce discrimination diagram for the subdivision of A-type granites (after Eby, 1992).

suite indicates that it did not result from Fe-Ti oxide fractional crystallization, because olivine and other minerals should crystallize before Fe-Ti oxides. It is more likely that the lithospheric mantle source of high-Ti mafic magmas continued to melt even after the source was largely depleted of Ti-bearing phases such as Cpx. This is consistent with the much lower abundances of REE and other trace elements in low-Ti vs. high-Ti suites (Fig. 9c, d). Support for this interpretation comes from the younger age of the low-Ti series (146 Ma) compared high-Ti series (153 Ma).

It should be emphasized that the high-Ti series is not unusual in a global sense; these have about average TiO_2 contents for basalts; their genesis requires no special explanation. In contrast, the low-Ti suite is globally unusual. These have TiO_2 and REE contents that are significantly lower than found for the most common, most-depleted igneous rock, MORB. Songhor low-Ti mafic melts are derived from an unusually depleted mantle source accompanied by degrees of magma contamination and fractionation. Their genesis requires a special explanation for how such an unusually depleted mantle could melt, as suggested above.

A negative correlation between MgO and SiO_2 (Fig. 8) may be attributed to olivine and pyroxene fractionation. In contrast, the high-Ti mafic group does not show any correlation among SiO_2-Al_2O_3 and SiO_2-TiO_2 pairs (Fig. 8), suggesting derivation of high-Ti rocks from

moderately fractionated magma. Associations between Ni and Cr (Supplementary Fig. 2a) suggest that basic magma was most affected by clinopyroxene crystallization. Fractionation of clinopyroxene is further supported by nearly constant Dy/Yb ratios with decreasing MgO contents (Supplementary Fig. 2b). The relatively flat HREE patterns of both basalt groups indicate a garnet-free source (Xu, 2001). Hence, mafic magmas were likely derived from spinel peridotite (Supplementary Fig. 2c). Weak Eu and Sr negative anomalies imply minor fractionation of plagioclase for high-Ti mafic rocks and low-Ti basalts, although low-Ti micro-gabbros/dolerites show strongly positive Eu and Sr anomalies (Fig. 9c, d). This indicates the fractionation of plagioclase in the evolution of low-Ti micro-gabbro/dolerite, because the mineral/melt partition coefficients for Sr and Eu in plagioclase are high, whereas the partition coefficients for other REE are low. In summary, the above observations indicate that both low-Ti basalts and micro-gabbros/dolerites were likely generated by similar parental magmas derived from partial melting of depleted mantle source and then fractional crystallization during magma evolution (Zeng et al., 2018). Low-Ti basalts were generated by lower degrees of partial melting followed by clinopyroxene accumulation, and low-Ti micro-gabbros/dolerites were generated by higher degrees of partial melting followed by fractionation of plagioclase and clinopyroxene (Zeng et al., 2018).

The correlation between La contents and La/Yb ratios implies a petrogenetic cause. The La/Yb ratio can be used to estimate melting depth (McKenzie and O'Nions, 1991). On the La/Yb versus Dy/Yb ratios diagram (Supplementary Fig. 2c), all Songhor mafic samples fall closest to the 5–10% melting of amphibole-spinel peridotite (Supplementary Fig. 2c). This is consistent with the partial melting of SCLM. Nd isotope ratios are consistent with this explanation. Coupled variations of T_{DM1} versus εNd(t) suggest that Songhor mafic magmas were derived from the partial melting of subcontinental lithospheric mantle (Fig. 10c). These mafic rocks show depleted and relatively homogeneous Sr-Nd isotopic compositions (Fig. 10a), arguing against significant crustal contamination.

Both high-Ti and low-Ti mafic groups fall in or near the field of oceanic island basalts (OIB) in the Sr-Nd isotope diagram (Fig. 10a). OIB generally plots below depleted mantle, while continental flood basalts overlap with OIB and range to lower εNd(t) and higher $^{87}Sr/^{86}Sr_{(i)}$, showing interaction/contamination with continental lithospheric mantle and/or crust (Qin et al., 2011).

The Nb/Yb-TiO_2/Yb plot of Pearce (2008) was used to constrain the source region of Songhor mafic rocks (Fig. 12a). This diagram shows the geochemical difference between low-Ti and high-Ti, ranging from N-MORB to OIB (Fig. 12a). Most low-Ti mafic rocks have Nb/Yb < 2 and

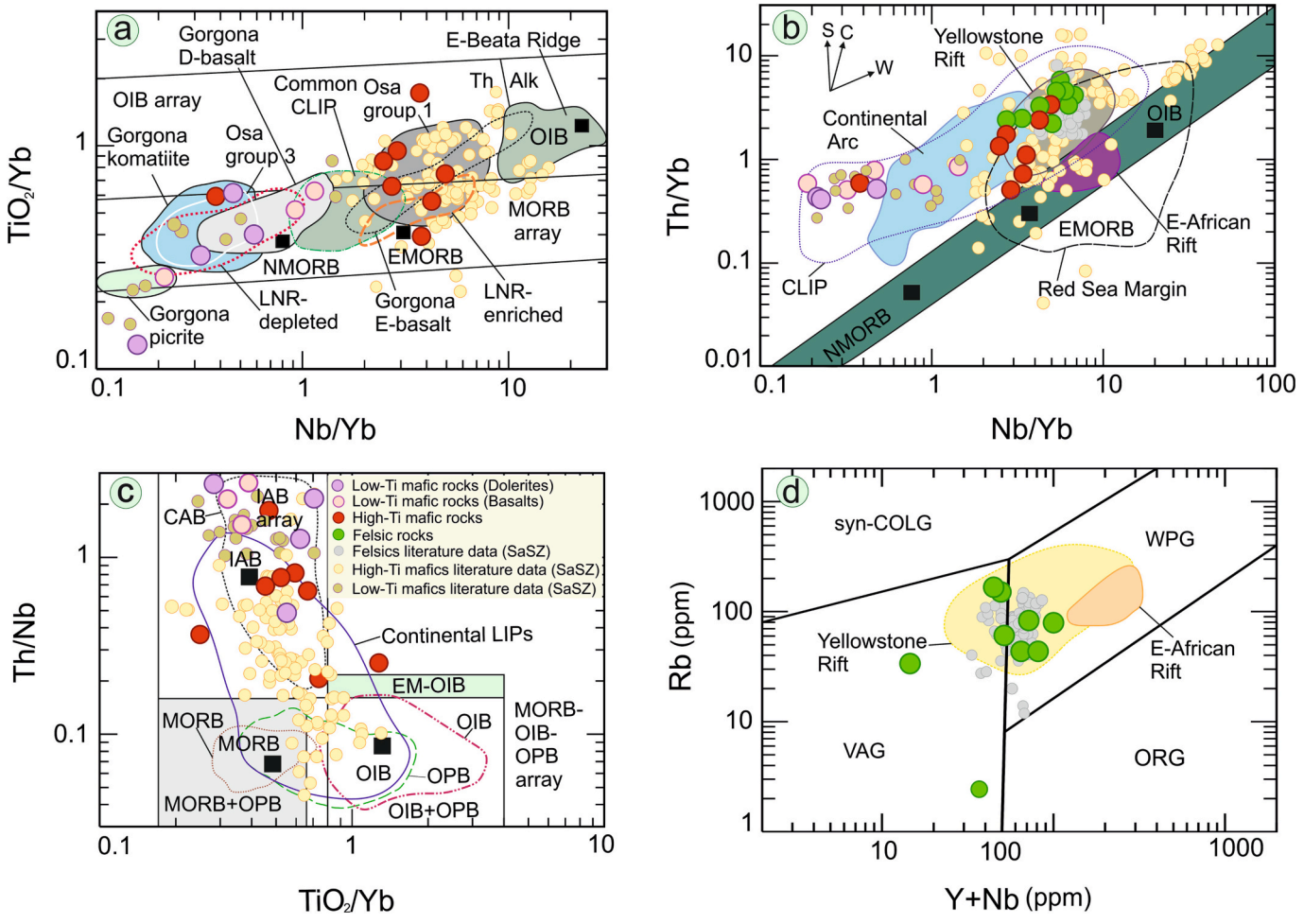

Fig. 12. **(a)** Nb/Yb versus TiO_2/Yb diagrams after Pearce (2008). Data for depleted samples from the Lower Nicaraguan Rise (LNR), E-Beata Ridge, Osa groups 1 and 3, Gorgona komatiites and picrites, depleted (D-) and enriched (E-) basalts from Dürkefälden et al. (2019a,b) and references therein. **(b)** Plot of Nb/Yb vs. Th/Yb (Pearce, 2008). MORB (PetDB at http://www.earthchem.org/petdb). PM: Primitive Mantle, UC: Upper Crust, OIB: Oceanic Island Basalt, S: Subduction, C: Continental crust, W: Within plate. The Songhor rocks show a distinct OIB signature and fall mainly in the fields of Yellowstone rift margin basalts (http://georoc.mpch-mainz.gwdg.de/georoc/). Continental arc basalt field from Pearce et al. (2021) and references therein. **(c)** Plot of TiO_2/Yb versus Th/Nb (Pearce et al., 2021). Data for different fields is from Pearce et al. (2021) and references therein. IAB: Island Arc Basalt, CAB: Continental Arc Basalt, CLIPs: Continental Large Igneous Provinces, OPB: Oceanic Plateau Basalt, EM: Enriched mantle. **(d)** Rb versus Y + Nb diagram (Pearce et al., 1984). The data from the East African and Yellowstone rift from the GEOROC database (http://georoc.mpch-mainz.gwdg.de/georoc/).

plot near normal mid-ocean ridge basalt (N-MORB) composition, as expected for these unusually depleted magmas. In contrast, the high-Ti mafic rocks have Nb/Yb > 2, similar to *E*-MORB, and are referred to as the enriched group (Fig. 12a). The depleted group is similar to some Cretaceous lavas from the Caribbean Large Igneous Province (CLIP) basalts, including Gorgona depleted (D-) basalts, nearby Lower Nicaraguan Rise depleted (LNR), Gorgona picrite and komatiite depleted Osa group 3 (Dürkefälden et al., 2019a, 2019b and references therein). In contrast, the enriched group is similar to enriched CLIP basalts like Osa Group 1 and Gorgona E-basalts (Dürkefälden et al., 2019a, 2019b and references therein). The process that generated Songhor mafic melts may be analogous to processes that produced those of CLIP.

A plot of Nb/Yb vs. Th/Yb is widely used to identify crustal contamination, but Songhor mafic samples show little evidence of this (Fig. 12b). The sample trend is similar to within-plate enrichment and/or fractional crystallization trends, but the samples are displaced to higher Th/Yb at lower Nb/Yb. Lower Nb/Yb contents for the depleted group may reflect the participation of Iran Cadomian lithospheric mantle, which formed over a S-dipping subduction zone in the Late Ediacaran/Early Cambrian time. Thus, lithospheric mantle modified by Cadomian subduction may be responsible for the strongly negative Ta, Nb, and Ti anomalies in Songhor igneous rocks, as suggested by Lightfoot et al. (1993) for the Siberian Noril'sk traps. In Fig. 12c, fields for MORB, OIB, OPB, and IAB are shown (with some overlap) on the TiO_2/Yb versus Th/Nb binary diagram. Although the data distribution in Fig. 12c demonstrates that LIP genesis involves many possible magma sources, Songhor high-Ti mafics lie in the field for continental LIPs but low-Ti mafics plot in the field of arc basalts.

6.3. Implications for tectonic setting and geodynamics

The Songhor region as a representative of the SaSZ shows close links between regional extension tectonics, rifting, and magma generation. The eruption of significant volumes of bimodal magmatic rocks suggests an extensional setting in Jurassic time. This could reflect continental rifting (Tian et al., 2019), continental back-arc extension, or post-orogenic extension (Jolivet et al., 2015). Magmatic rocks corresponding to these different tectonic regimes have different geochemical features. On a basis of geochemistry alone, Songhor rocks could have formed in a back-arc basin because these have geochemical characteristics transitional from N-MORB to arc or calc-alkaline basalts (Cui et al., 2020). However, a back-arc basin requires an accompanying magmatic arc and fore arc of similar and older ages, but none is known from this region. A post-orogenic extensional setting is also not favored because this requires that an episode of crustal thickening occurred just before; in fact, the previous orogenic event – the collision of Iran with Asia – occurred ~100 m.y. before SaSZ and Songhor igneous activity. This leaves continental rifting as the remaining likely explanation.

Formation in a Late Jurassic continental rift is consistent with the bimodal nature of Songhor igneous rocks. Felsic lavas are intercalated with mafic lavas and intruded by plutons of similar bimodal composition. The felsic rocks are predominantly metaluminous to peraluminous and have moderately high εNd(t) values (+0.6 to +3.8) that overlap with the isotopic ratios of the mafic rocks. It is generally accepted that A-type felsic magmas form in rifting or extensional environments (Eby, 1992; Whalen et al., 1987). However, it is often difficult to address the specific tectonic setting of A-type granites/rhyolites because of their similar lithology, mineralogy, and geochemistry (Sylvester, 1998).

Eby (1992) subdivided A-type granites into A1 and A2 groups. A1-granites originate from differentiation of OIB-like magmas, whereas A2-granites are regarded as partial melting products of lower continental crust. Most Songhor felsic rocks belong to the A2 subdivision (Eby, 1992), which occurs in a variety of tectonic environments including arc and post-orogenic environments, where magmas are derived from the crustal or underplated mafic crust (Fig. 11f). Some Songhor samples show affinities to A1-A2 boundary and A1 field.

In the Y + Nb vs. Rb discrimination diagram (Pearce et al., 1984) most Songhor felsics plot in the within plate field (Fig. 12d), similar to granites from the Songhor-Ghorveh area (Azizi et al., 2020b; Maanijou et al., 2013). Geochemical features indicate that Songhor felsic rocks are similar to those of typical intracontinental extension settings. Their intracontinental extension setting is further corroborated because Songhor felsic rocks mostly cluster in the intraplate type A-granite field (Fig. 12d) on the Y + Nb vs. Rb discrimination diagram (Pearce et al., 1984); Th/Yb–Nb/Yb systematics of felsic rocks (Fig. 12b) suggests a component associated with mantle plumes (Wyman and Kerrich, 2012). When the REE patterns and spider diagrams of Songhor rocks are compared with those of two modern continental LIPs in both mafic and felsic samples share geochemical similarities with lavas from those two intra-plate locations (Fig. 9). On the Rb vs. Y + Nb diagram, Songhor felsic lavas are similar to those of Yellowstone (Fig. 12d; http://georoc.mpch-mainz.gwdg.de/georoc/) and show modest Nb-Ta depletions suggesting more crustal interaction than those from the East African Rift, but the overall patterns are comparable.

Songhor igneous rocks are graphically compared (Fig. 12b, d) to those of the Red Sea margin, Yellowstone hotspot, and East African Rift. In the Th/Yb versus Nb/Yb diagram (Fig. 12b: after Pearce, 2008), most high-Ti mafic rocks show a distinctive OIB signature similar to igneous rocks of those three igneous provinces. In contrast, some low-Ti micro-gabbros/dolerites plot in the arc field (Pearce, 2008). OIB-mantle origin is also confirmed by La/Yb versus Th/Ta ratios and La-Y-Nb (Cabanis and Lecolle, 1989) for most Songhor mafic rocks (Supplementary Fig. 3a, b), which also plot close to the fields of Deccan and Siberian LIPs.

An arc-like trace element signature is identified for high-field-strength elements (HFSEs: Nb, Ta, Ti, and Zr) anomalies in Songhor low-Ti mafic series; these are similar to arc-like basalts in the Siberian, Central Atlantic, and southern Karoo LIPs (http://georoc.mpch-mainz.gwdg.de/georoc/). Pearce et al. (2021) noted that intraplate basalts can plot in the arc or intraplate fields depending on the relative contributions of asthenosphere, metasomatized lithosphere, and continental crust in their genesis.

Some geochemical discrimination diagrams misidentify intra-continental basaltic rocks with similar HFSE depletions as arc-related (Wang et al., 2016), especially for continental flood basalt (CFB) provinces (Wang et al., 2016 and references therein). These signatures reflect ancient lithospheric memories. Wang et al. (2016) suggest that the best discrimination diagrams for distinguishing arc-like CFBs are Ti versus V and Sr/Nd-Zr/Sm-Ti/V ternary plots (Supplementary Fig. 3c, d). Songhor mafic rocks show similar affinities with arc-like basalts from other CFBs. Arc-like CFBs define a trend mostly along the Ti/V to Zr/Sm boundary, whereas true arc basalts define a trend toward Sr enrichment that is nearly perpendicular to the trend of arc-like continental basalts (Supplementary Fig. 3c, d). In this case, most Songhor rocks show a similar trend to that of CFBs whereas more evolved micro-gabbros and/or dolerites follow the arc trend.

These considerations further indicate that Songhor mafic magmas were derived from the lithospheric mantle, perhaps with some interaction of asthenospheric OIB-like melts. Our data suggest that Songhor felsic magmas are derived by remelting of underplated lower crust with minor crustal mixing-assimilation. Fig. 13 shows the interaction of mantle and crustal melts decreasing toward the N in Iran. This suggests that the continental crust thinned southwestward in the C-SaSZ during Jurassic time.

We think that Songhor Jurassic magmatism was generated as transitional crust in a volcanic rifted passive continental margin on the northern margin of Neo-Tethys. Strong extension with normal and listric faulting on the western margin of the C-SaSZ thinned Iranian continental lithosphere leading to extensive SCLM partial melting. The association of alkaline to tholeiitic mafic and felsic magmatic rocks with shallow to deep marine facies sedimentary layers in the Songhor basin is like that of a volcanic passive margin prior to continental break-up. The presence of

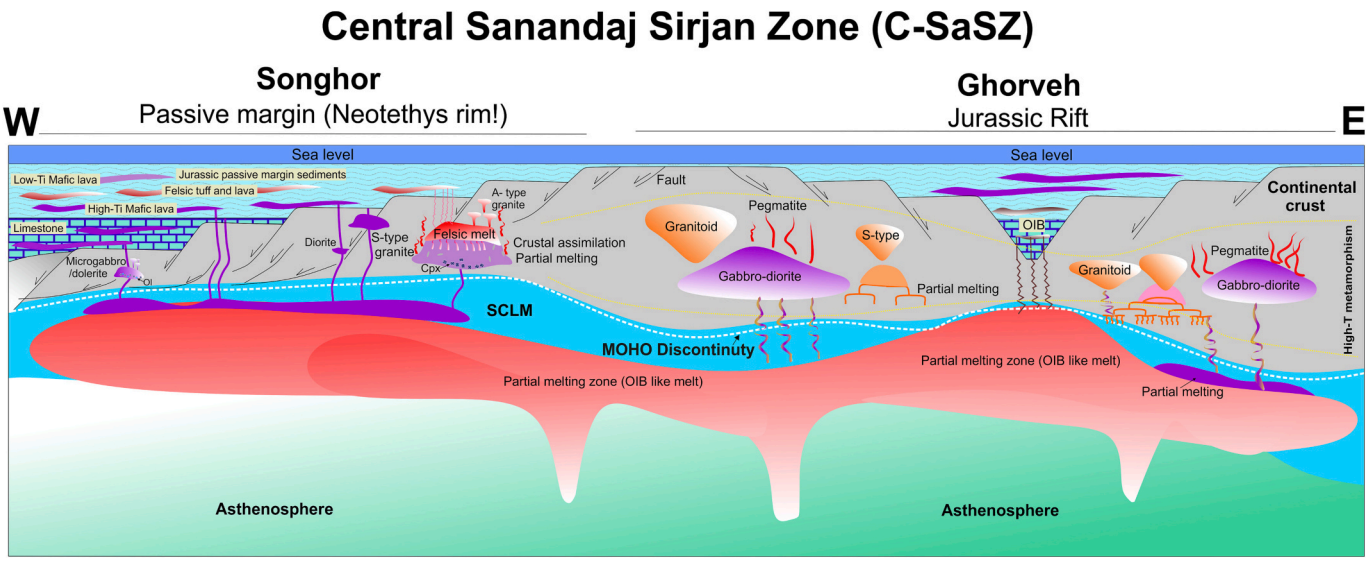

Fig. 13. Development of a passive continental margin in western Iran in Jurassic time. Extension associated with magmatism and normal and listric faults shaped transitional crust from the C-SaSZ to Neo-Tethys oceanic crust. Thinning of the lithosphere triggered partial melting of the subcontinental lithospheric mantle. In the first stage when the crust was thicker, remelting of mafic underplate and minor crust generated A-type granitic melts. Continued extension generated large volumes of basaltic melts which erupted in shallow marine basins.

Jurassic rift-related magmatic rocks unconformably overlain by Early Cretaceous marine sediments is expected. The formation of passive continental margin begins with tectonic extension that is generally accompanied by igneous activity (Robertson et al., 2020); this phase is followed by thermal subsidence with little or no igneous activity as the affected lithosphere heals and thickens; a video showing the evolution of a continental rift into a passive margin can be seen at (https://www.youtube.com/watch?v=W6oJKsSiLEI). The location of the Songhor region at the southern limit of Iran continental crust and its evolution from Jurassic rift-related igneous rocks to Early Cretaceous marine sediments is well explained by interpreting Jurassic igneous rocks of the SaSZ as the magmatic expression of a new passive continental margin (Fig. 13). Further studies focused on how Jurassic and Early Cretaceous igneous and sedimentary rocks vary in selected NE-SW oriented transects across the SaSZ are needed to test this hypothesis.

7. Conclusions

Songhor magmatic rocks constitute a bimodal magmatic suite, with a significant compositional gap between mafic and felsic members. Magmatism took place over ~10 Ma in Late Jurassic time, with felsic magma generated first (156 Ma) followed by alkali basalts (153 Ma) and then unusually depleted tholeiites (146 Ma). Mafic rocks consist of high- and low -Ti series, although both share a common isotopic character and related trace element signatures. The low-Ti suite is younger and less fractionated, with Mg# between 55 and 74 compared to 43 to 63 for the older high-Ti basaltic rocks. High-Ti basalts exhibit slightly alkaline chemistry and affinity to typical classical continental rift environments, such as those of the East African Rift. Low-Ti mafic magmas show arc-like HFSE signatures but mostly have similar geochemical signatures to recent plume- and rift-related magmatic rocks. In the Songhor area in Late Jurassic time, mantle-derived melts contributed heat for crustal melting and minor interaction with continental crust to produce felsic melts. Thinning of continental lithosphere continued and partial melting of SCLM derived mafic melts to produce high-Ti basaltic magmas. It is more likely that the lithospheric mantle source of high-Ti mafic magma continued to partially melt even after the source was largely depleted of Ti-bearing phases such as Cpx, to produce low-Ti volcanic and hyp-abyssal rocks.

Declaration of Competing Interest

The authors declare that they have no known competing financial interests or personal relationships that could have appeared to influence the work reported in this paper.

Acknowledgments

This research was supported by the University of Kurdistan, Iran, and Nagoya University, Japan. A part of this work was supported by the Japan Society for Promotion of Sciences (JSPS) KAKENHI grant numbers 17H011671 and 18H05447. We are grateful to F. Rezaei, A. Mohammadi, and E. Fathi for field work and technical assistance. This is UTD Geoscience Contribution. #16xx. This version benefitted greatly from the critical comments from editor Prof. N. Malaspina and three anonymous reviewers.

Appendix A. Supplementary data

Supplementary data to this article can be found online at https://doi.org/10.1016/j.lithos.2023.107023.

References

Anh, T.V., Pang, K.N., Chung, S.L., Lin, H.M., Hoa, T.T., Anh, T.T., Yang, H.J., 2011. The Song Da magmatic suite revisited: a petrologic, geochemical and Sr–Nd isotopic study on picrites, flood basalts and silicic volcanic rocks. J. Asian Earth Sci. 42, 1341–1355. https://doi.org/10.1016/j.jseaes.2011.07.020.

Ayalew, D., Gibson, S.A., 2009. The head-to-tail transition of the Afar mantle plume: geochemical evidence from a Miocene bimodal basalt–rhyolite succession in the Ethiopian large Igneous Province. Lithos 112, 461–476. https://doi.org/10.1016/j.lithos.2009.04.005.

Azizi, H., Asahara, Y., 2013. Juvenile granite in the Sanandaj-Sirjan Zone, NW Iran: late Jurassic-early cretaceous arc-continent collision. Int. Geol. Rev. 55, 1523–1540. https://doi.org/10.1080/00206814.2013.782959.

Azizi, H., Stern, R.J., 2019. Jurassic igneous rocks of the Central Sanandaj-Sirjan zone (Iran) mark a propagating continental rift, not a magmatic arc. Terra Nova 31, 415–423. https://doi.org/10.1111/ter.12404.

Azizi, H., Asahara, Y., Mehrabi, B., Chung, S.L., 2011. Geochronological and geochemical constraints on the petrogenesis of high-K granite from the Suffi abad area, Sanandaj-Sirjan Zone, NW Iran. Chem. Erde-Geochem. 71, 363–376. https://doi.org/10.1016/j.chemer.2011.06.005.

Azizi, H., Najari, M., Asahara, Y., Catlos, E.J., Shimizu, M., Yamamoto, K., 2015a. U-Pb zircon ages and geochemistry of Kangareh and Taghiabad mafic bodies in northern Sanandaj-Sirjan Zone, Iran: evidence for intra-oceanic arc and back-arc tectonic

regime in late Jurassic. Tectonophys. 660, 47–64. https://doi.org/10.1016/j.tecto.2015.08.008.
Azizi, H., Zanjefili-Beiranvand, M., Asahara, Y., 2015b. Zircon U-Pb ages and petrogenesis of a tonalite–trondhjemite–granodiorite (TTG) complex in the northern Sanandaj Sirjan zone, Northwest Iran: evidence for late Jurassic arc-continent collision. Lithos 216, 178–195. https://doi.org/10.1016/j.lithos.2014.11.012.
Azizi, H., Lucci, F., Stern, R.J., Hasannejad, S., Asahara, Y., 2018. The late Jurassic Panjeh submarine volcano in the northern Sanandaj-Sirjan Zone, Northwest Iran: Mantle plume or active margin. Lithos 308–309, 364–380. https://doi.org/10.1016/j.lithos.2018.03.019.
Azizi, H., Nouri, F., Stern, R.J., Azizi, M., Lucci, F., Asahara, Y., Zarinkoub, M.H., Chung, S.L., 2020a. New evidence for Jurassic continental rifting in the northern Sanandaj Sirjan Zone, western Iran: the Ghalaylan seamount, southwest Ghorveh. Int. Geol. Rev. 62, 1635–1657. https://doi.org/10.1080/00206814.2018.1535913.
Azizi, H., Asahara, Y., Minami, M., Anma, R., 2020b. Sequential magma injection with a wide range of mixing and mingling in late Jurassic plutons, southern Ghorveh, western Iran. J. Asian Earth Sci. 200, 104469 https://doi.org/10.1016/j.jseaes.2020.104469.
Barth, A.P., Wooden, J.L., Tosdal, R.M., Morrison, J., 1995. Crustal contamination in the petrogenesis of a calc–alkalic rock series: Josephine Mountain intrusion, California. Geol. Soc. Am. Bull. 107 (2), 201–212. https://doi.org/10.1130/0016-7606(1995)107%3C0201:CCITPO%3E2.3.CO;2.
Brewer, T.S., Ahall, K.I., Menuge, J.F., Storey, C.D., Parrish, R.R., 2004. Mesoproterozoic bimodal volcanism in SW Norway, evidence for recurring pre-Sveconorwegian continental margin tectonism. Precambrian Res. 134, 249–273. https://doi.org/10.1016/j.precamres.2004.06.003.
Brophy, J.G., 2008. A study of rare earth element (REE)-SiO2 variations in felsic liquids generated by basalt fractionation and amphibole melting: a potential test for discrimination between the two different processes. Contrib. Mineral. Petrol. 156, 337–357. https://doi.org/10.1007/s00410-008-0289-x.
Cabanis, B., Lecolle, M., 1989. Le diagramme La/10-Y/15-Nb/8: un outil pour la discrimination des séries volcaniques et la mise en évidence des processus de mélange et/ou de contamination crustale. Comptes rendus de l'Académie des sciences. Série 2. Mécanique, Physique, Chimie, Sciences de l'univers, Sciences de la Terre 309, 2023–2029.
Castillo, P.R., Liu, X., Scarsi, P., 2020. The geochemistry and Sr-Nd-Pb isotopic ratios of high 3He/4He Afar and MER basalts indicate a significant role of the African Superplume in EARS magmatism. Lithos 376, 105791. https://doi.org/10.1016/j.lithos.2020.105791.
Corti, G., 2009. Continental rift evolution: from rift initiation to incipient break-up in the Main Ethiopian Rift, East Africa. Earth Sci. Rev. 96, 1–53. https://doi.org/10.1016/j.earscirev.2009.06.005.
Cui, X., Sun, M., Zhao, G., Yao, J., Zhang, Y., Han, Y., Dai, L., 2020. A Devonian arc–back-arc basin system in the southern Chinese Altai: constraints from geochemical and Sr-Nd-Pb isotopic data for meta-basaltic rocks. Lithos 366, 105540. https://doi.org/10.1016/j.lithos.2020.105540.
Davoudian, A.R., Genser, J., Dachs, E., Shabanian, N., 2008. Petrology of eclogites from north of Shahrekord, Sanandaj-Sirjan Zone, Iran. Mineral. Petrol. 92, 393–413. https://doi.org/10.1007/s00710-007-0204-6.
Dostal, J., Wilson, R.A., Jutras, P., 2021. Petrogenesis of Siluro-Devonian rhyolites of the Tobique Group in the northwestern Appalachians (northern New Brunswick, Canada): tectonic implications for the accretion history of peri-Gondwanan terranes along the Laurentian margin. Geol. Soc. Lond. Spec. Publ. 391-407 https://doi.org/10.1144/SP503-2019-229.
Dürkefälden, A., Hoernle, K., Hauff, F., Wartho, J.A., van den Bogaard, P., Werner, R., 2019a. Age and geochemistry of the Beata Ridge: primary formation during the main phase (~ 89 Ma) of the Caribbean large Igneous Province. Lithos 328, 69–87. https://doi.org/10.1016/j.lithos.2018.12.021.
Dürkefälden, A., Hoernle, K., Hauff, F., Werner, R., Garbe-Schönberg, D., 2019b. Second-stage Caribbean large Igneous Province volcanism: the depleted icing on the enriched cake. Chem. Geol. 509, 45–63. https://doi.org/10.1016/j.chemgeo.2019.01.004.
Eby, G.N., 1992. Chemical subdivision of the A-type granitoids: petrogenetic and tectonic implications. Geol. 20, 641–644. https://doi.org/10.1130/0091-7613(1992)020%3C0641:CSOTAT%3E2.3.CO;2.
Eshraghi, S.A., Jafarian, M.B., Eghlimi, B., 1996. Geological Map of Songhor 1:100,000. Geol. Surv, Iran.
Gholipour, S., Azizi, H., Masoudi, F., Asahara, Y., Tsuboi, M., 2021. Zircon U-Pb ages, geochemistry, and Sr-Nd isotope ratios for early cretaceous magmatic rocks, southern Saqqez, northwestern Iran. Chemie der Erde-Geochem. 125687 https://doi.org/10.1016/j.chemer.2020.125687.
Hosseiny, M., 1999. Geological Map of Ghorveh, Scale 1/100000, No. 5560. Geological Survey of Iran.
Hunziker, D., Burg, J.P., Bouilhol, P., von Quadt, A., 2015. Jurassic rifting at the Eurasian Tethys margin: Geochemical and geochronological constraints from granitoids of North Makran, southeastern Iran. Tecton. 34, 71–593. https://doi.org/10.1002/2014TC003768.
Jolivet, L., Gorini, C., Smit, J., Leroy, S., 2015. Continental breakup and the dynamics of rifting in back-arc basins: the Gulf of Lion margin. Tecton. 34, 662–679. https://doi.org/10.1002/2014TC003570.
Li, L., Lin, S., Xing, G., Davis, D.W., Davis, W.J., Xiao, W., Yin, C., 2013. Geochemistry and tectonic implications of late Mesoproterozoic alkaline bimodal volcanic rocks from the Tieshajie Group in the southeastern Yangtze Block, South China. Precambrian Res. 230, 179–192. https://doi.org/10.1016/j.precamres.2013.02.004.
Lightfoot, P.C., Hawkesworth, C.J., Hergt, J., Naldrett, A.J., Gorbachev, N.S., Fedorenko, V.A., Doherty, W., 1993. Remobilisation of the continental lithosphere by a mantle plume: major-, trace-element, and Sr-, Nd-, and Pb-isotope evidence from picritic and tholeiitic lavas of the Noril'sk District, Siberian Trap, Russia. Contrib. Mineral. Petrol. 114, 171–188. https://doi.org/10.1007/BF00307754.
Lyu, P.L., Li, W.X., Wang, X.C., Pang, C.J., Cheng, J.X., Li, X.H., 2017. Initial breakup of supercontinent Rodinia as recorded by ca 860–840 Ma bimodal volcanism along the southeastern margin of the Yangtze Block, South China. Precambrian Res. 296, 148–167. https://doi.org/10.1016/j.precamres.2017.04.039.
Ma, L., Jiang, S.Y., Hofmann, A.W., Dai, B.Z., Hou, M.L., Zhao, K.D., Chen, L.H., Li, J.W., Jiang, Y.H., 2014. Lithospheric and asthenospheric sources of lamprophyres in the Jiaodong Peninsula: a consequence of rapid lithospheric thinning beneath the North China Craton? Geochim. Cosmochim. Acta 124, 250–271. https://doi.org/10.1016/j.gca.2013.09.035.
Maanijou, M., Aliani, F., Miri, M., Lentz, D.R., 2013. Geochemistry and petrology of igneous assemblage in the south of Qorveh area, West Iran. Chemie der Erde-Geochem. 73, 181–196. https://doi.org/10.1016/j.chemer.2013.04.001.
Mahmoudi, S., Corfu, F., Masoudi, F., Mehrabi, B., Mohajjel, M., 2011. U-Pb dating and emplacement history of granitoid plutons in the northern Sanandaj-Sirjan Zone: Iran. J. Asian Earth Sci. 41, 238–249. https://doi.org/10.1016/j.jseaes.2011.03.006.
Mahoney, J.J., Saunders, A.D., Storey, M., Randriamanantenasoa, A., 2008. Geochemistry of the Volcan de l'Androy basalt–rhyolite complex, Madagascar cretaceous igneous province. J. Petrol. 49, 1069–1096. https://doi.org/10.1093/petrology/egn018.
McKenzie, D.A.N., O'Nions, R.K., 1991. Partial melt distributions from inversion of rare earth element concentrations. J. Petrol. 32, 1021–1091. https://doi.org/10.1093/petrology/32.5.1021.
Melluso, L., Mahoney, J.J., Dallai, L., 2006. Mantle sources and crustal input as recorded in high-Mg Deccan Traps basalts of Gujarat (India). Lithos 89, 259–274. https://doi.org/10.1016/j.lithos.2005.12.007.
Middlemost, E.A.K., 1994. Naming materials in the magma/igneous rock system. Earth Sci. Rev. 37, 215–224.
Natali, C., Beccaluva, L., Bianchini, G., Siena, F., 2011. Rhyolites associated to Ethiopian CFB: clues for initial rifting at the Afar plume axis. Earth Planet. Sci. Lett. 312, 59–68. https://doi.org/10.1016/j.epsl.2011.09.059.
Orihashi, Y., Nakai, S.I., Hirata, T., 2008. U-Pb age determination for seven standard zircons using inductively coupled plasma–mass spectrometry coupled with frequency quintupled Nd-YAG (λ= 213 nm) laser ablation system: comparison with LA-ICP-MS zircon analyses with a NIST glass reference material. Resour. Geol. 58, 101–123. https://doi.org/10.1111/j.1751-3928.2008.00052.x.
Patiño Douce, A.E., 1997. Generation of metaluminous A-type granites by low-pressure melting of calc-alkaline granitoids. Geol. 25, 743–746. https://doi.org/10.1130/0091-7613(1997)025%3C0743:GOMATG%3E2.3.CO;2.
Patiño Douce, A.E., Beard, J.S., 1995. Dehydration-melting of biotite gneiss and quartz amphibolite from 3 to 15 kbar. J. Petrol. 36, 707–738. https://doi.org/10.1093/petrology/36.3.707.
Pearce, J.A., 2008. Geochemical fingerprinting of oceanic basalts with applications to ophiolite classification and the search for Archaean oceanic crust. Lithos 100, 14–48. https://doi.org/10.1016/j.lithos.2007.06.016.
Pearce, J.A., Harrison, N.B.W., Tindle, A.G., 1984. Trace element discrimination diagrams for the tectonic interpretation of granitic rocks. J. Petrol. 25, 956–983.
Pearce, N.J.G., Perkins, W.T., Westgate, J.A., Gorton, M.P., Jackson, S.E., Neal, C.R., Chenery, S.P., 1997. A compilation of new and published major and trace element data for NIST SRM 610 and NIST SRM 612 glass reference materials. Geostand. Newslett. 21, 115–144. https://doi.org/10.1111/j.1751-908X.1997.tb00538.x.
Pearce, J.A., Ernst, R.E., Peate, D.W., Rogers, C., 2021. LIP printing: use of immobile element proxies to characterize large Igneous Provinces in the geologic record. Lithos 392-393, 106068. https://doi.org/10.1016/j.lithos.2021.106068.
Peccerillo, A., Taylor, S.R., 1976. Geochemistry of Eocene calc-alkaline volcanic rocks from the Kastamonu area, northern Turkey. Contrib. Mineral. Petrol. 58, 63–81.
Qin, K.Z., Su, B.X., Sakyi, P.A., Tang, D.M., Li, X.H., Sun, H., Xiao, Q.H., Liu, P.P., 2011. SIMS zircon U-Pb geochronology and Sr-Nd isotopes of Ni-Cu-Bearing Mafic-Ultramafic intrusions in Eastern Tianshan and Beishan in correlation with flood basalts in Tarim Basin (NW China): Constraints on a ca. 280 Ma mantle plume: American. J. Dermatol. Sci. 311, 237–260. https://doi.org/10.2475/03.2011.03.
Rahimzadeh, B., Mahmoudi, S., Corfu, F., Ahadnejad, V., Von Quadt, A., 2021. A unique period of bimodal volcanism at 130–110 Ma in the northern Sanandaj-Sirjan Zone: evidence for an extensional setting. Lithos 392, 106155. https://doi.org/10.1016/j.lithos.2021.106155.
Robertson, A.H., Parlak, O., Kinnaird, T.C., Taslı, K., Dumitrica, P., 2020. Cambrian-Eocene pre-rift, pulsed rift, passive margin and emplacement processes along the northern margin of the Southern Neotethys: evidence from the Antalya complex in the Alanya Window (S Turkey). J. Asian Earth Sci. 3, 100026 https://doi.org/10.1016/j.jaesx.2020.100026.
Rudnick, R.L., Gao, S., Holland, H.D., Turekian, K.K., 2003. Composition of the continental crust. Crust 3, 1–64.
Schmandt, B., Dueker, K., Humphreys, E., Hansen, S., 2012. Hot mantle upwelling across the 660 beneath Yellowstone. Earth Planet. Sci. Lett. 331, 224–236. https://doi.org/10.1016/j.epsl.2012.03.025.
Sharma, M., Basu, A.R., Nesterenko, G.V., 1992. Temporal Sr-, Nd- and Pb-isotopic variations in the Siberian flood basalts: Implications for the plume-source characteristics. Earth Planet. Sci. Lett. 113, 365–381. https://doi.org/10.1016/0012-821X(92)90139-M.
Shellnutt, J.G., Wang, C.Y., Zhou, M.F., Yang, Y., 2009. Zircon Lu–Hf isotopic compositions of metaluminous and peralkaline A-type granitic plutons of the Emeishan large igneous province (SW China): constraints on the mantle source. J. Asian Earth Sci. 35, 45–55. https://doi.org/10.1016/j.jseaes.2008.12.003.

Shellnutt, J.G., Bhat, G.M., Wang, K.L., Brookfield, M.E., Dostal, J., Jahn, B.M., 2012. Origin of the silicic volcanic rocks of the early Permian Panjal Traps, Kashmir, India. Chem. Geol. 334, 154–170. https://doi.org/10.1016/j.chemgeo.2012.10.022.

Shinjo, R., Chung, S.L., Kato, Y., Kimura, M., 1999. Geochemical and Sr-Nd isotopic characteristics of volcanic rocks from the Okinawa Trough and Ryukyu Arc: Implications for the evolution of a young, intracontinental back arc basin. J. Geophys. Res. Solid Earth 104, 10591–10608. https://doi.org/10.1029/1999JB900040.

Stacey, J.S., Kramers, J.D., 1975. Approximation of terrestrial lead isotope evolution by a two-stage model. Earth Planet. Sci. Lett. 26, 207–221. https://doi.org/10.1016/0012-821X(75)90088-6.

Stefano, T., Mariano, P., Stefano, V., Alessandro, I., Amerigo, C., Cinzia, B., Stefano, M., 2018. Early Jurassic rifting of the Arabian passive continental margin of the Neo-Tethys. Field evidence from the Lurestan region of the Zagros fold-and-thrust belt. Iran. Tecton. 37, 2586–2607. https://doi.org/10.1029/2018TC005192.

Stein, M., Hofmann, A.W., 1992. Fossil plume head beneath the Arabian lithosphere? Earth Planet. Sci. Lett. 114, 193–209. https://doi.org/10.1016/0012-821X(92)90161-N.

Stern, R.J., 2002. Crustal evolution in the East African Orogen: a neodymium isotopic perspective. J. Afr. Earth Sci. 34, 109–117. https://doi.org/10.1016/S0899-5362(02)00012-X.

Stern, R.J., Moghadam, H.S., Pirouz, M., Mooney, W., 2021. The Geodynamic Evolution of Iran. Annual Rev. Earth Planet. Sci. Lett. 49, 9–36. https://doi.org/10.1146/annurev-earth-071620-052109.

Stocklin, J., Nabavi, M.H., 1973. Tectonic map of Iran. Geol. Surv. Iran. 1, 5.

Sun, S.S., McDonough, W.F., 1989. Chemical and isotopic systematics of oceanic basalts: implications for mantle composition and processes. Geol. Soc. Lond. Spec. Publ. 42, 313–345.

Sylvester, P.J., 1998. Post-collisional strongly peraluminous granites. Lithos 45, 29–44. https://doi.org/10.1016/S0024-4937(98)00024-3.

Tanaka, T., Togashi, S., Kamioka, H., Amakawa, H., Kagami, H., Hamamoto, T., Yuhara, M., Orihashi, Y., Yoneda, S., Shimizu, H., Kunimaru, T., Takahashi, K., Yanagi, T., Nakano, T., Fujimaki, H., Shinjo, R., Asahara, Y., Tanimizu, M., Dragusanu, C., 2000. JNdi-1: a neodymium isotopic reference in consistency with LaJolla neodymium. Chem. Geol. 168, 279–281.

Tao, Y., Bi, X., Li, C., Hu, R., Li, Y., Liao, M., 2014. Geochronology, petrogenesis and tectonic significance of the Jitang granitic pluton in eastern Tibet, SW China. Lithos 184, 314–323. https://doi.org/10.1016/j.lithos.2013.10.031.

Tavakoli, N., Shabanian, N., Davoudian, A.R., Azizi, H., Neubauer, F., Asahara, Y., Bernroider, M., Lee, J.K., 2021. A-type granite in the Boein-Miandasht complex: evidence for a late Jurassic extensional regime in the Sanandaj-Sirjan Zone, western Iran. J. Asian Earth Sci. 213, 104771 https://doi.org/10.1016/j.jseaes.2021.104771.

Thy, P., Beard, J.S., Lofgren, G.E., 1990. Experimental constraints on the origin of Icelandic rhyolites. J. Geol. 98, 417–421.

Tian, D., Yang, H., Ge, W., Zhang, Y., Chen, J., Chen, H., Yun, X., 2018. Petrogenesis and tectonic implications of late Carboniferous continental arc high-K granites in the Dongwuqi area, Central Inner Mongolia, North China. J. Asian Earth Sci. 167, 82–102. https://doi.org/10.1016/j.jseaes.2018.07.010.

Tian, Y., Gong, J., Chen, H., Guo, L., Xu, Q., Chen, L., Lin, X., Cheng, X., Yang, R., Zhao, L., Yang, S., 2019. Early cretaceous bimodal magmatism in the eastern Tethyan Himalayas, Tibet: Indicative of records on precursory continental rifting and initial breakup of eastern Gondwana. Lithos 324, 699–715. https://doi.org/10.1016/j.lithos.2018.12.001.

Turner, S., Rushmer, T., 2009. Similarities between mantle-derived A-type granites and voluminous rhyolites in continental flood basalt provinces. Earth Environ. Sci. Trans. Royal Soc. Edinburgh 100, 51–60.

Wang, X.C., Wilde, S.A., Xu, B., Pang, C.J., 2016. Origin of arc-like continental basalts: Implications for deep-Earth fluid cycling and tectonic discrimination. Lithos 261, 5–45. https://doi.org/10.1016/j.lithos.2015.12.014.

Whalen, J.B., Hildebrand, R.S., 2019. Trace element discrimination of arc, slab failure, and A-type granitic rocks. Lithos 348–349. https://doi.org/10.1016/j.lithos.2019.105179.

Whalen, J.B., Currie, K.L., Chappell, B.W., 1987. A-type granites: geochemical characteristics, discrimination and petrogenesis. Contrib. Mineral. Petrol. 95, 407–419. https://doi.org/10.1007/BF00402202.

Wiedenbeck, M., Hanchar, J.M., Peck, W.H., Sylvester, P., Valley, J., Whitehouse, M., Kronz, A., Morishita, Y., Nasdala, L., Fiebig, J., Franchi, I., Girard, J.P., Greenwood, R.C., Hinton, R., Kita, N., Mason, P.R.D., Norman, M., Ogasawara, M., Piccoli, P.M., Rhede, D., Satoh, H., Schulz-Dobrick, B., Skår Spicuzza, M.J., Terada, K., Tindle, A., Togashi, S., Vennemann, T., Xie, Q., Zheng, Y.F., 2004. Further characterisation of the 91500-zircon crystal. Geostandards and Geo. Res. 28, 9–39. https://doi.org/10.1111/j.1751-908X.2004.tb01041.x.

Wyman, D.A., Kerrich, R., 2012. Geochemical and isotopic characteristics of Youanmi terrane volcanism: the role of mantle plumes and subduction tectonics in the western Yilgarn Craton. Austral. J. Earth Sci. 59, 671–694. https://doi.org/10.1080/08120099.2012.702684.

Xu, Y.G., 2001. Thermo-tectonic destruction of the Archean lithospheric keel beneath the Sino-Korean Craton in China: evidence, timing and mechanism: Physics and Chemistry of the Earth. Part A. Solid Earth Geod. 26, 747–757. https://doi.org/10.1016/S1464-1895(01)00124-7.

Yajam, S., Montero, P., Scarrow, J.H., Ghalamghash, J., Razavi, S.M.H., Bea, F., 2015. The spatial and compositional evolution of the late Jurassic Ghorveh-Dehgolan plutons of the Zagros Orogen, Iran: SHRIMP zircon U-Pb and Sr and Nd isotope evidence. Geol. Acta: Int. Earth Sci. J. 13, 25–43.

Zarasvandi, A., Rezaei, M., Raith, J.G., Lentz, D.R., 2021. Why are there no Cu-porphyry deposits in Jurassic Sanandaj-Sirjan zone intrusions of Iran? Int. Geol. Rev. 1-15 https://doi.org/10.1080/00206814.2020.1864792.

Zeng, L., Zhang, K.J., Tang, X.C., Zhang, Y.X., Li, Z.W., 2018. Mid-Permian rifting in Central China: record of geochronology, geochemistry and Sr–Nd–Hf isotopes of bimodal magmatism on NE Qinghai–Tibetan Plateau. Gondwana Res. 57, 77–89. https://doi.org/10.1016/j.gr.2017.12.013.

Zhu, J., Zhang, Z., Santosh, M., Tan, S., Deng, Y., Xie, Q., 2021. Recycled carbon degassed from the Emeishan plume as the potential driver for the major end-Guadalupian carbon cycle perturbations. Geosci. Front. 12, 101140 https://doi.org/10.1016/j.gsf.2021.101140.

Further reading

Zhang, Z., Xiao, W., Ji, W., Majidifard, M.R., Rezaeian, M., Talebian, M., Xiang, D., Chen, L., Wan, B., Ao, S., Esmaeili, R., 2018. Geochemistry, zircon U-Pb and Hf isotope for granitoids, NW Sanandaj-Sirjan zone, Iran: implications for Mesozoic-Cenozoic episodic magmatism during Neo-Tethyan lithospheric subduction. Gondwana Res. 62, 227–245. https://doi.org/10.1016/j.gr.2018.04.002.